A preserved record of early solar system melting in the carbonaceous achondrites Northwest Africa 7680 and 6962

Brendt C. Hyde[a,b,*], Desmond E. Moser[a], Kimberly T. Tait[b], James R. Darling[c], Qing-Zhu Yin[d], Matthew E. Sanborn[d], Neil R. Banerjee[a,e], Arshad Ali[a,f], Iffat Jabeen[a] and Hugo Moreira[c]

[a]Department of Earth Sciences, University of Western Ontario, London, Ontario, N6A 5B7, Canada
[b]Department of Natural History, Royal Ontario Museum, Toronto, Ontario, M5S 2C6, Canada
[c]School of the Environment, Geography and Geosciences, University of Portsmouth, Portsmouth PO13QL, UK.
[d]Department of Earth and Planetary Sciences, University of California Davis, One Shields Avenue, Davis, California 95616, USA
[e]Institute for Earth and Space Exploration, University of Western Ontario, London, Ontario, N6A 5B7, Canada
[f]Earth Sciences Research Centre (ESRC), Sultan Qaboos University, Al-Khoudh, Muscat 123, Sultanate of Oman
*Corresponding author email address: b.hyde@queensu.ca, present address: Department of Geological Sciences and Geological Engineering, Queen's University, Kingston, Ontario, K7L 3N6, Canada

Keywords: NWA 7680, NWA 6962, carbonaceous achondrite, early solar system geochronology, thermochronology

ABSTRACT

The carbonaceous achondrites Northwest Africa (NWA) 7680 and NWA 6962 have been investigated for their texture, mineralogy, geochemistry and geochronology. The major, minor and trace element compositions of the mineral components, oxygen isotope and chromium isotope compositions, along with U-Pb ratio phosphate thermochronology suggest that they were formed by similar processes on the same parent body. The achondrites have olivine compositions of $Fa_{44.8}$ and $Fa_{47.4}$ for NWA 7680 and NWA 6962 respectively. Replicate oxygen isotope analyses of grains and bulk powders from NWA 7680 yielded average $\Delta^{17}O$ values of -1.04‰ ± 0.03 and -1.00 ± 0.05‰ respectively, which is identical to that reported for NWA 6962. The whole rock $\varepsilon^{54}Cr$ compositions are also equivalent for NWA 7680 and NWA 6962 (1.36 ± 0.05 and 1.30 ± 0.05 respectively). Both meteorites are plagioclase-rich, and NWA 7680 is also Fe-metal-rich, suggesting they both formed via differentiation processes that resulted in the pooling of partial melt products. Major element geochemical trends show that both rocks could be formed through melting of chondritic material on a CR chondrite-like parent body. This is consistent with oxygen isotope and chromium isotope compositions. Intrusion of a late-stage

melt is evident in both meteorites and the melt products include silica-rich, alkali-deficient nepheline. The late-stage liquid has re-melted and mixed with primary plagioclase in NWA 6962. In contrast, the late-stage liquid was often restricted to grain boundaries in NWA 7680, leaving some of the primary plagioclase crystals intact. *In situ* dating of NWA 7680 phosphate minerals (merrillite and fluorapatite) reveals that it has not experienced long duration thermal metamorphism, or impact related Pb loss and age resetting since 4578 ± 17 Ma ($^{207}Pb/^{206}Pb$ age ± 2σ, within error of solar system age). Phosphates associated with the late-stage melt in NWA 6962 yield a $^{207}Pb/^{206}Pb$ age of 4556.6 ± 8.0 Ma (2σ) within 2σ of the NWA 7680 age. Thermochronology data confirms that the observed chromium isotope signatures in these meteorites were not introduced by a later high temperature event, such as late impact accretion processes. These data are consistent with a rapid separation of inner and outer solar system chemical reservoirs, planetesimal melting, differentiation and cooling, all within several million years of calcium aluminum-rich inclusion (CAI) formation.

INTRODUCTION

Evidence for early melting, crystallization and differentiation processes within asteroidal bodies is provided by the measured ages of the oldest differentiated meteorites including the iron meteorite Steinbach dated at 4565.47 ± 0.30 Ma (Connelly et al. 2019), as well as meteorites representing silica-rich basaltic melts: Asuka 881394 at 4564.95 ± 0.53 Ma (Wimpenny et al. 2019) and NWA 11119 at 4564.8 ± 0.3 Ma (Srinivasan et al. 2018). The crystallization of some of these early differentiation products was taking place contemporaneously with chondrule formation (4567.32 ± 0.42 to 4564.71 ± 0.30 Ma, Connelly et al. 2012). Early melt rocks from carbonaceous chondrite-like parent bodies have also been found and include NWA 6704 and NWA 6693, which have Pb-isotopic ages of 4562.76 ± 0.22/0.30 Ma and 4562.63 ± 0.29/0.21 Ma respectively (Amelin et al. 2019; Sanborn et al. 2019). The discovery of these and other carbonaceous achondrites have added to the known diversity of materials associated with the solar system's formative melt environments. The preserved record of some of these unique and early carbonaceous chondrite-like melts will be the focus of this study.

The study of carbonaceous chondrite-like melts is essential for our knowledge of the spatial distribution and types of melt environments in the evolving solar system. The early solar system experienced a segregation of two distinct chemical reservoirs, the carbonaceous chondrite-like (outer solar system) materials and non-carbonaceous (inner solar system) materials (e.g., Warren 2011; Sanborn and Yin, 2019). This means that our only knowledge of early outer solar system asteroidal melt environments comes from the carbonaceous achondrites and iron meteorites associated with this reservoir (e.g., Nanne et al. 2019). Isotopic distinctions for these two reservoirs are observed in many elements including Cr (e.g., Trinquier et al. 2007; Warren 2011; Sanborn et al. 2019), Ti (e.g., Leya et al. 2008; Trinquier et al. 2009; Warren 2011), Mo (e.g., Budde et al. 2016) and Ni (Nanne et al. 2019). The most probable and effective way to separate these two reservoirs was through the rapid formation of Jupiter (Kruijer et al.

2017; Nanne et al. 2019). Kruijer et al. (2017) argued that Jupiter's core grew to ~20 Earth masses in less than one million years. The source of the isotopic differences appears, at least in some cases, to be related to the input of distinct source materials into the outer solar system. Studies of the carbonaceous chondrite Orgueil show enrichments in ^{54}Cr associated with sub-micrometer Cr-rich grains (likely Cr-spinels). These enrichments are thought to be directly produced in supernovae (Dauphas et al. 2010; Qin et al. 2011). Similarly, the Mo isotopic anomalies seen in meteorites also require contributions from distinct supernovae processes (Yin et al. 2002).

The existence of the carbonaceous chondrite-like and non-carbonaceous reservoirs, alongside geochronological data, provides a powerful tool for reconstructing processes occurring in the early solar system. The separation of these reservoirs also makes it strikingly obvious that little is known about differentiation processes in the outer solar system, since most of the collected meteoritic material from the carbonaceous chondrite-like reservoir is in the form of primitive carbonaceous chondrites and iron meteorites associated with carbonaceous chondrites (e.g., Nanne et al. 2019). Stable isotope studies of some stony igneous meteorites have linked them to outer solar system carbonaceous chondrite-like parent bodies (e.g., Sanborn and Yin 2019; Sanborn et al. 2019). In particular, there have been multiple carbonaceous achondrites with stable isotopic compositions similar to those of CR chondrites. These carbonaceous achondrites include NWA 6704 and NWA 6693 (Warren et al. 2013; Amelin et al. 2019; Hibiya et al. 2019; Sanborn et al. 2019), NWA 2976 and NWA 011 (Bogdanovski and Lugmair 2004; Sanborn et al. 2013) and Tafassasset (Gardner-Vandy et al. 2012; Sanborn et al. 2019). These meteorites provide a rare opportunity to characterize and date melting and differentiation processes in outer solar system materials.

This study focuses on the formation environments and ages of the carbonaceous achondrites NWA 7680 and NWA 6962. Although they are not paired, initial observations note geochemical, textural and mineralogical similarities between these two meteorites (Ruzicka et al. 2015a; Ruzicka et al. 2015b). We present major, minor and trace element compositions of the mineral constituents along with U-Pb ratio phosphate thermochronology, oxygen isotope compositions and chromium isotope compositions. These data help determine if the two meteorites are from the same parent body and allow for comparisons with other carbonaceous achondrites, including those with CR affinities. The results of this study will place constraints on early melt generation in the outer solar system and the timeline for planet formation.

SAMPLES AND ANALYTICAL METHODS

Meteorite Samples

The type specimen for NWA 7680 and NWA 6962 were first characterized in 2013 and 2012, respectively (Ruzicka et al. 2015a; Ruzicka et al. 2015b). The samples of NWA 7680 and NWA 6962 used in this study were acquired from the collection of the Royal Ontario Museum (ROM) and are catalogued under the numbers M57074 and M56452, respectively. The entire

NWA 7680 meteorite was purchased in Tucson in 2011 and donated to the ROM. Material from NWA 6962 was then purchased by the ROM for comparative analysis. Two thick sections and one etched slab (Fig. 1) of NWA 7680 were used for *in situ* analysis, along with one thick section of NWA 6962. Oxygen isotope analyses used loose grains and bulk powders of NWA 7680.

Backscatter Electron Imaging, Chemical Mapping, Modal Analysis and Cathodoluminescence

Backscatter electron (BSE) imaging, chemical mapping and cathodoluminescence (CL) were carried out using a Hitachi SU6600 Field Emission Scanning Electron Microscope (FE-SEM) at the University of Western Ontario. An Oxford XMax silicon drift detector (80 mm^2) was used for energy dispersive spectrometry (EDS) measurements. Modal analysis used the INCA software package, which utilizes ternary plots to specify phase compositions within element maps. A Gatan Chroma CL detector was used with an accelerating voltage of 10 kV and a working distance of roughly 12.8 mm, which was adjusted for optimal emission/detection. Emissions were binned into 4 channels: red (600–850 nm), green (500–600 nm), blue (400–500 nm), and ultraviolet (300–400 nm) and images were assembled using the Gatan Digital Micrograph software.

Raman Spectroscopy

Raman spectra were acquired using a Horiba LabRAM ARAMIS micro-Raman spectrometer at the ROM. A 532 nm, 50 mW laser was used, but was filtered to 1.64 mW to prevent sample damage. A 1200 groove/mm grating and 100 µm slit were used during collection. A Si reference material was used for calibration. Two spectra were collected for 50 s at each point and the results were averaged. The RRUFF Raman database and CrystalSleuth (Lafuente et al. 2016) were used for rapid identification, followed by literature comparisons.

Electron Probe Microanalysis

Electron probe microanalysis (EPMA) using wavelength dispersive spectrometry (WDS) was conducted at Queen's University on a JEOL JXA-8230 equipped with five wavelength dispersive spectrometers. All analyses used a 15 kV accelerating voltage. A beam current of 10 nA was used for merrillite analyses, 20 nA beam was used for silicate, fluorapatite and chromite analyses and 30 nA was used for metal and sulfides. Standards used for microprobe analyses are given in the Supporting Information online (Table S1). A spot size of 7 µm and 14 µm were used for fluorapatite and a Na-rich silicate respectively. Analysis of the Durango apatite standard showed no noticeable change in F Kα X-ray count rate over a period of 10 minutes with the set-up used for fluorapatite in these samples. Time dependant analyses were carried out for fluorapatite (F) as well as the Na-rich silicate (Na) using the Probe for EPMA software package to process the data. Chromite Fe(II) to Fe(III) calculations used an iterative procedure in which Fe(III) was calculated by charge balance, and then matrix corrections were recalculated. This

procedure was repeated until the resulting changes were below the uncertainty levels for measured Fe.

Trace Element and U-Pb Isotope Ratio Analyses

Laser ablation inductively coupled plasma mass spectrometry (LA-ICP-MS) data were collected as a time series using two systems. Trace elements were measured on an Agilent 7500cs (quadrupole) ICP-MS system with a New-Wave UP213 (213 nm) solid-state Nd:YAG laser. Olivine, pyroxene and plagioclase were analyzed with spot sizes of 30-100 μm, a laser repetition rate of 10 Hz and fluence of 3.6-5.0 J cm^{-2}. The ablation cell was flushed with He gas flow of 1 L/min and Ar was introduced before reaching the torch. Analytical runs consisted of 15 s of background and 25 s of ablation. Background and sample intervals were selected using SILLS software (Guillong et al. 2008). Each LA-ICP-MS analysis was normalized to CaO as measured by EPMA. Replicate LA-ICP-MS analyses of the NIST 612 standard were run after 3-7 sample analyses to correct for drift. Sample analyses were also bracketed by measurements of NIST 614 which yielded an accuracy of better than ±7.3% error (average of 37 analyses) for all reported measurements.

Additional trace element characterization and U-Pb isotope ratio analyses were carried out using an Analytic Jena Plasma Quant MS Elite ICP-MS with an ASI RESOlution SE 193 nm excimer laser. Phosphate, plagioclase and pyroxene were analyzed with spot sizes of 25-50 μm, a laser repetition rate of 4 Hz and a fluence of 4-4.5 J cm^{-2} to obtain trace element concentrations. Uranium-lead isotopic ratio measurements on phosphates were carried out with spot sizes of 20-30 μm, a laser repetition rate of 2-4 Hz and fluence of 2.5-4 J cm^{-2}. To correct for instrumental mass bias and within-run drift, analyses were normalized to the 473.5 ± 0.7 Ma Madagascar fluorapatite (Thomson et al. 2012), which was measured each 2-3 sample analyses. The primary Madagascar analyses were corrected for variable common lead correction using a ^{207}Pb correction (Chew et al. 2014). Durango apatite and McClure apatite were measured as secondary reference materials to monitor accuracy and precision, yielding lower intercept ages of 31.9 ± 6.8 Ma and 503 ± 26 Ma respectively on a Tera-Wasserburg plot, which are within 2σ of reference values (McDowell et al. 2005; Thomson et al. 2012).

Oxygen Isotope Analyses

Acid-washed bulk powders and cleaned grain separates were used for triple oxygen isotope analysis at the University of Western Ontario. The grains used were predominantly olivine; however, chromite inclusions were common and unavoidable. Associated plagioclase was also a likely minor constituent in the samples. The laser line and methodology used in this study are similar to that used in Ali et al. (2016) and Ali et al. (2018). The reader is directed to these studies for a more thorough description of methodology; however, a brief description is provided here. The laser line used is equipped with a 25 W 10.6 μm CO_2 laser (Model MIR10-25) and a custom-designed sample holder (Ali et al. 2016; Ali et al. 2018). The laser line was prepared the night before the analytical session. One to two milligrams of dried sample was

placed in the sample wells and the sample holder was placed in the reaction chamber. The samples were preheated to 110 °C overnight under vacuum. After cooling the sample chamber, prefluorination with BrF_5 was carried out for at least 3 h. The laser heating was carried out in a stepwise fashion starting with a defocused wide beam and increasing focus and laser power over time. After each laser reaction, the liberated O_2 gas was separated and purified using cryogenic methods and a KCl trap. Finally, the O_2 gas was adsorbed using 5 Å molecular sieve at liquid nitrogen temperature (-196 °C). To further purify this oxygen from any NF_3 impurities, the molecular sieve trap was heated using an ethanol-liquid N_2 bath to -100 °C and pure oxygen gas released was then collected in a separate tube by readsorption onto a 5 Å molecular sieve using liquid nitrogen. This O_2 gas was then analyzed using a Delta V Plus mass spectrometer in dual inlet mode with Isodat3.0 software. External precision (1SE) was determined from eight individual runs of UWG-2 (Valley et al. 1995) in a single day, which provided an external precision of ±0.04‰ $\delta^{17}O$ and ±0.08‰ in $\delta^{18}O$.

Chromium Isotope Analyses

Chromium isotopic compositions were measured in sub-samples of fusion crust-free whole rock fractions of NWA 7680 and NWA 6962. Small chips of each meteorite were crushed in a mortar and pestle, homogenized, and then an aliquot of each was taken for processing (8.14 mg for NWA 7680 and 16.90 mg for NWA 6962). Each fraction was placed into PTFE parr bomb digestion vessels along with a 3:1 mixture of HF and HNO_3 and sealed in stainless-steel jackets. The parr bombs were placed into a 190°C for 96 hours. The high pressure-temperature conditions dissolve all phases, including refractory components. After dissolution, the whole-rock fractions were dried down and treated with alternating steps of 6 N HCl and concentrated nitric acid to break down any fluorides formed during the digestion process. The dissolved material was processed through a 3-column separation procedure described in detail by Yamakawa et al. (2009) in a class 10/100 cleanroom at the University of California, Davis (UC Davis). Chromium isotopic measurements were made on the purified Cr fractions using a Thermo *Triton Plus* thermal ionization mass spectrometer at UC Davis. A total of 12 mg of Cr was loaded evenly across four outgassed W filaments for a total load of 3 mg per filaments. Two filaments loaded with 3 mg of the NIST SRM 979 Cr standard were analyzed before and after each set of four sample filaments. For each filament, a total of 1200 ratios were analyzed with an 8 second integration time for each ratio. A gain was measured at the start of every filament and a baseline measured every 25 ratios. Each filament was set to maintain a signal of 10 V (± 15%) on ^{52}Cr using a 10^{11}-ohm resistor. Mass fractionation was corrected for using an exponential law and a $^{50}Cr/^{52}Cr$ ratio of 0.051859 (Shields et al., 1966). The $^{54}Cr/^{52}Cr$ ratios are reported as parts per 10,000 deviations (epsilon units) from the measured NIST SRM 979 standard.

RESULTS

Petrography

NWA 7680 is metal-rich (57.3 area %) with a silicate portion composed of roughly mm-scale olivine grains (35.6 %) with interstitial feldspar (6.0 %) (Fig. 2). Upon etching, the metallic portion of the meteorite exhibits polygonal crystals with well-defined edges. Linear bands are visible within individual metal crystals and never cross grain boundaries (Fig. 1). Clinopyroxene (<0.1 %) is present as a minor phase and is often found along grain boundaries associated with sulfide (0.5 %) and a Na-rich silicate (<0.1 %). The Na-rich silicate is a minor component. Raman spectra of the phase are consistent with a nepheline-tridymite-like mineral (Fig. 3). The grouping of peaks between 950 and 1050 cm^{-1} seen in both NWA 7680 and NWA 6962 is diagnostic for nepheline suggesting this is the most likely identity; however, the dominant peak at 400-415 cm^{-1} always contains a shoulder similar to the peak splitting seen in tridymite (Fig. 3). Chromite (0.5 %) is also found throughout the section, along with minor merrillite and fluorapatite (0.1 % phosphate) (Fig. 4). NWA 6962 has olivine (70 %) similar in size to NWA 7680; however, in this case, the interstitial spaces are a mixture of feldspar (19.9 %), clinopyroxene (4.2 %) and merrillite (3.6 % phosphate) (Fig. 2 and Fig. 4). The clinopyroxene is more ubiquitous in NWA 6962 and exhibits complex zonation and is often anhedral or subhedral. Chromite (1.7 %), sulfide (0.3 %), metal (0.2 %), minor fluorapatite and a Na-rich silicate (Fig 2d) are also found in the section. Trace amounts of micrometer-scale zirconium-phases are also found in the both meteorites, usually associated with the Na-rich silicate. The most common phase is baddeleyite, but zirconolite is also seen in NWA 7680.

Mineral Compositions

All average mineral compositions for NWA 7680 and NWA 6962 can be found in Tables 1 and 2, respectively, except for the extremely variable feldspar compositions, which are in the Supporting Information online (Table S2). NWA 7680 contains Fe-metal grains multiple millimeters across with a median Ni content of 5.99 wt.% (Fig. 1). Small regions with distinct boundaries and high Ni content are found within these grains with concentrations as high as 57.38 wt.%. The olivine is homogeneous ($Fa_{44.8 \pm 0.2}$, Fig. 5, Table 1) with notable Ca content (Fig. 6, 0.47 ± 0.05 wt.% CaO) and Fe/Mn (apfu ratio) value of 72.6 ± 2.8, while the feldspar shows a variable composition ($An_{2.1\text{-}51.1}Or_{1.0\text{-}83.7}$, Fig. 7, Table S2). The K-rich feldspar is rare and generally found along grain boundaries. Clinopyroxene grains generally have minimal zonation; however, some have zones of varying composition ($Fs_{11.0\text{-}22.8}Wo_{46.6\text{-}48.6}$, Fig. 5). Clinopyroxene is often found along grain boundaries and associated with sulfide and Na-rich silicate. The chemistry of the Na-rich silicate, along with its Raman spectrum, identifies the phase as silica-rich, alkali-deficient nepheline (Dollase and Thomas 1978). Chromite has an average Fe_2O_3 content of 1.66 wt.%. The Ti content is quite variable (3.09 ± 1.29(1σ), Table 1). Generally, the centre of large grains has a TiO_2 content of less than 3 wt.%, whereas grain edges and chromite inclusions have higher concentrations, reaching as high as 5.32 wt.%. The Fe-

sulfides have pyrrhotite-group compositions and a minor Ni-rich-sulfide is also present. The Cl content in the fluorapatite is below detection limits and element totals suggest that the hydroxyl group (OH) is less than 1 wt.%, if it is present. The merrillite has a notable quantity of FeO (average = 1.41 wt.%).

NWA 6962 also contains largely homogeneous olivine ($Fa_{47.4\pm0.3}$, 0.43±0.06 wt.% CaO, Fe/Mn = 72.0 ± 3.4, Fig. 5 and Fig. 6), consistent with past studies (Ruzicka et al. 2015a; Dunlap et al. 2015). However, along edges of one anhedral grain, a more Mg-rich composition is seen (Fig. 5). Recent analyses of another section of NWA 6962 has shown reverse chemical zoning with similar Mg-enrichment (Abe et al. 2021), suggesting that there may be variability within the available NWA 6962 material. Olivine grains are mainly associated with a mixture of feldspar ($An_{4.1\text{-}33.9}Or_{0.2\text{-}3.3}$, Fig. 7), clinopyroxene ($Fs_{11.9\text{-}23.4}Wo_{42.3\text{-}48.7}$, Fig. 5) and merrillite (Table 2). Chromite has an average Fe_2O_3 content of 1.76 wt.%. The Ti content is similar to that of NWA 7680 in some respects with large grain centres generally having a TiO_2 content of less than 3 wt.%; however, grain edges and chromite inclusions have even higher concentrations, reaching as high as 11.94 wt.%. Rare anhedral grains of titanian chromite are also observed (TiO_2 = 14.68–18.74 wt.%). The sulfides have pyrrhotite-group compositions. Metal in NWA 6962 has a notably lower Ni content (median value of 1.39 wt.%) than that of NWA 7680 (Fig. 8). The merrillite is again Fe-rich (FeO average = 1.02 wt.%). In some areas, the merrillite has developed a sponge-like texture (Fig. 4f) and analyses return low totals. The minor fluorapatite contains measurable Cl (sub wt.%) and appears to be anhydrous. The Na-rich silicate in NWA 6962 is also silica-rich, alkali-deficient nepheline (Fig. 3).

Rare Earth Element Compositions

Trace element compositions were measured for phosphates, plagioclase, olivine, and pyroxene in both NWA 7680 and NWA 6962 (Fig. 9, Table S3). The phosphates have a heavy rare earth element (HREE)-depleted pattern with a negative Eu anomaly (Fig. 9a). Both merrillite and fluorapatite have similar rare earth element (REE) patterns for both samples; however, merrillite generally has higher REE concentrations than fluorapatite. Plagioclase also appears to have a HREE-depleted pattern (Fig. 9a); however, some elements were below detection limits for the examined grains. The plagioclase in both samples has a positive Eu anomaly. Olivine in both NWA 7680 (Fig. 9b) and NWA 6962 (Fig. 9c) generally have light rare earth element (LREE)-depleted patterns for the elements that were above the detection limits. Pyroxene in NWA 7680 (Fig. 9b) has a relatively flat REE pattern, while most NWA 6962 grains have LREE-depleted patterns and have negative Eu anomalies (Fig. 9c).

Oxygen and Chromium Isotope Characteristics

Olivine grain separates (minor chromite and plagioclase) gave average oxygen isotope compositions of $\delta^{17}O = 2.39 \pm 0.12$; $\delta^{18}O = 6.58 \pm 0.17$; $\Delta^{17}O = -1.04‰ \pm 0.03$ (n = 5, all uncertainties are 2 SE). Acid-washed bulk powders gave average values of $\delta^{17}O = 3.07 \pm 0.25$; $\delta^{18}O = 7.80 \pm 0.40$; $\Delta^{17}O = -1.00 \pm 0.05‰$ (n = 3, all uncertainties are 2 SE) (Fig. 10 and 11).

Whole rock fractions of NWA 7680 and NWA 6962 gave $\varepsilon^{54}Cr$ compositions of 1.36 ± 0.05 and 1.30 ± 0.05 respectively. These data have been plotted alongside known chondrite and achondrite compositions (Fig. 12).

U-Pb and ^{207}Pb-^{206}Pb ages

Measurements of U-Pb ratios were taken from eleven spots in NWA 7680. Ten of the spots were from merrillite grains (four different grains) and one spot was from fluorapatite (Table 3, Fig. 13a and Fig. 13b). Seven spots were measured in NWA 6962. Four of the spots were merrillite grains (4 different grains) and three spots were from fluorapatite (1 grain) (Table 3, Fig. 13c and Fig. 13d). The data (Table 3) have been plotted on Tera-Wasserburg plots for examination (Fig. 13). One spot from NWA 7680 produced a $^{207}Pb/^{206}Pb$ age and uncertainty that place it as chronologically older than CAIs (Connelly et al. 2012). Texturally there is no reason to suggest the grain is presolar, and we consider that this reflects incorporation of (uncorrected) common-Pb. With this point removed, the weighted mean $^{207}Pb/^{206}Pb$ age for NWA 7680 is 4578 ± 17 Ma (uncertainty at 95% confidence level, MSWD = 1.01, probability = 0.43). All the data from NWA 6962 are concordant or near concordant and the resulting weighted mean $^{207}Pb/^{206}Pb$ age is 4556.6 ± 8.0 Ma (uncertainty at 95% confidence level, MSWD = 0.62, probability = 0.71).

Discussion

Comparisons with Achondrite Groups

The mineralogical and geochemical similarities suggest that NWA 7680 and NWA 6962 are from the same parent body. Major and minor element composition in NWA 7680 and NWA 6962 olivine and pyroxene (Fig. 5 and Fig. 6) along with oxygen isotope compositions (Fig. 10 and Fig. 11) suggest no direct relationship with established achondrite groups. Oxygen isotope values are within the range of known ureilites and acapulcoites/lodranites (Fig. 11); however, olivine compositions from NWA 7680 and NWA 6962 are more FeO-rich than currently known meteorites from either of these groups (Fig. 5). The oxygen isotope compositions also place them near the CR chondrite trend line (Fig. 10). Minor element compositions in olivine (Fig. 6) do not suggest a direct relation to either the ureilites or acapulcoites/lodranites.

Trace element data for the phases in NWA 7680 and NWA 6962 provide an additional means of comparison to ureilites and acapulcoites/lodranites. The clinopyroxene REE compositions of NWA 7680 and NWA 6962 are dependent on their formation mechanism. Pyroxene that nucleated along olivine grain boundaries or replaced olivine (Fig. 2d) have flatter REE patterns. The pyroxene grains in NWA 7680 are all formed in this manner (Fig. 9b). One pyroxene region measured in NWA 6962 exhibited the same flat pattern; however, the majority of grains in NWA 6962 formed in association with plagioclase, in a later stage melt. Pyroxene forming with plagioclase exhibit a negative Eu anomaly (Fig. 9c), while associated plagioclase contains a positive Eu anomaly (Fig. 9a). The pyroxene patterns for NWA 6962 are somewhat similar to those of acapulcoites-lodranites; however, the NWA 6962 grains exhibit smaller Eu

anomalies (Fig. 9c; Floss 2000; Guan and Crozaz 2000, 2001). The NWA 6962 pyroxene compositions are actually similar to compositions from augite in carbonaceous chondrites (e.g., Jacquet et al. 2012). These compositions are consistent with a primitive parent body for NWA 7680 and NWA 6962. Concentrations of REE are above those expected for ureilite clinopyroxene and olivine (Fig. 9b and Fig. 9c, Guan and Crozaz, 2000; Guan and Crozaz 2001).

A Link to Carbonaceous Chondrites

The chromium isotope compositions alongside the previously mentioned oxygen isotope compositions confirm a carbonaceous (outer solar system) origin for NWA 7680 and NWA 6962 and suggest a CR chondrite-like reservoir (Fig. 10 and Fig. 12). Olivine minor element compositions from NWA 7680 and NWA 6962 overlap with metamorphic clasts from CM (Zhang et al. 2010) and CV (Jogo et al. 2013) chondrites (Fig. 6). These clasts have some mineralogic similarities to NWA 7680 and NWA 6962. They are olivine-rich, most contain plagioclase and pyroxene, and some contain nepheline and/or merrillite as well as chromite, Fe-Ni-metal and sulfides including pyrrhotite and pentlandite (Zhang et al. 2010; Jogo et al. 2013). However, the olivine grains in these clasts are smaller and have lower FeO content (Fa_{34-39}) than those in NWA 7680 and NWA 6962. These clasts have a range of oxygen isotope compositions falling near the carbonaceous chondrite anhydrous mineral (CCAM) line. These clasts may have all originated from the interior of the CV parent body, with impacts relocating some of these materials to the CM parent body (Zhang et al. 2010; Jogo et al. 2013). Another material with mineralogic similarities to NWA 7680 and NWA 6962 is the feldspar-nepheline (FELINE) clast found in the Parnallee LL 3.6 chondrite (Bridges et al. 1995). This clast is nepheline-rich (12 modal %) and has an oxygen isotope composition that also falls near the CCAM line (Bridges et al. 1995). The REE compositions from the FELINE feldspar match those from NWA 7680 and NWA 6962 (Fig. 9).

The chromium and oxygen isotope measurements alongside evidence for similar materials in carbonaceous chondrites negate the possibility that NWA 7680 and NWA 6962 are geochemically unique meteorites from the ureilite or acapulcoite/lodranite parent bodies. However, these well-studied meteorite groups and their formation environments provide useful data for comparison with the carbonaceous achondrites. Using a modal recombination to mimic bulk compositions, it is apparent that, geochemically, both NWA 7680 and NWA 6962 can be formed through fractionation processes on a CR chondrite-like parent body (Fig. 14). This simple fractionation trend and the identification of similar clasts in carbonaceous chondrites suggest that melts similar to NWA 7680 and NWA 6962 may be common amongst carbonaceous chondrite parent bodies. The fractionation trend seen in Fig. 14 intersects the solar photosphere composition and falls near other primitive carbonaceous chondrite compositions (CI, CM and CO). Partial melting of CR chondrite-like starting material could produce residual materials with some geochemical similarities to the ureilites, lodranites-acapulcoites and brachinites (Fig. 14); however, these materials would have distinctly different chromium isotope compositions (Fig. 12).

The CR Chondrite-Like Reservoir

Since NWA 7680 and NWA 6962 formed in a CR chondrite-like reservoir, examining the onset of thermal metamorphism and melting of similar materials is a starting point in determining their formation environment. The majority of CR chondrites show little or no evidence of thermal metamorphism (e.g., Briani et al. 2013); however, there are meteorites that have been interpreted as highly equilibrated chondrites from a CR chondrite-like reservoir and some have been confirmed through chromium and oxygen isotope analysis (NWA 3100, NWA 2994, NWA 6921 and NWA 7317; Sanborn et al. 2019 and references therein). Both NWA 3100 and NWA 2994 (paired with NWA 6921 and NWA 7317) contain remnant chondrules (Bunch et al. 2008). The modal mineralogy for NWA 3100 and NWA 2994 is dominated by olivine and orthopyroxene (nearly 90%; Bunch et al. 2005; Bunch et al. 2008). These textures and mineralogies are distinct from those seen in NWA 7680 and NWA 6962. Since the thermal histories of NWA 7680 and NWA 6962 have advanced past this initial stage of equilibration use of the term "carbonaceous achondrite" as a description would be appropriate. The other carbonaceous achondrites with CR chondrite-like isotopic signatures vary considerably in terms of rock type and mineralogy. NWA 011 and NWA 2976 are paired pigeonite-plagioclase-rich basaltic achondrites (Yamaguchi et al. 2002), NWA 6704 and NWA 6693 are paired meteorites that are pyroxene-rich, with less abundant olivine, feldspar and minor phases (Warren et al. 2013; Hibiya et al. 2019). Tafassasset has some variability in its mineralogy, but is generally olivine-pyroxene-rich (e.g., Gardner-Vandy et al. 2012). It differs from the other carbonaceous achondrites discussed because one relict chondrule has been found (Bourot-Denise et al. 2002). These carbonaceous achondrites suggest substantial diversity in the types of melts produced in the CR chondrite-like reservoir. Below we will further compare these meteorites in terms of their formation and use olivine compositions and bulk REE compositions as points of comparison.

As mentioned in the previous section, both NWA 7680 and NWA 6962 can be formed through fractionation processes on a CR chondrite-like parent body and most likely formed through a high degree of partial melting of CR chondrite-like material (Fig. 14). Continued melting and fractionation could lead to increasingly Mg-poor, Al-rich materials and eventually basaltic compositions. Basalts can deviate from a given fractionation line towards higher Al-compositions as seen with terrestrial basalts (Fig, 14). This is also observed with the pigeonite-plagioclase-rich basaltic carbonaceous achondrite NWA 011 (Fig. 14), leaving open the possibility that NWA 011 (and NWA 2976) could be derived from a similar parent body to NWA 7680 and NWA 6962. However, NWA 011 olivine has a higher iron content ($Fa_{79.5\text{-}81.4}$), higher Fe/Mn value (108) and slightly lower CaO content (0.2 wt.%) (Floss et al. 2005) than that of NWA 7680 and NWA 6962. The carbonaceous achondrites NWA 6704 and NWA 6693 experienced more complex histories in the early solar nebula (Fig. 14 and Hibiya et al. 2019), have bulk geochemical signatures that cannot be directly associated with fractionation through partial melting (Fig. 14), have low CaO (<0.08 wt.%) concentrations and higher Fe/Mn values in their olivine (Warren et al. 2013; Hibiya et al. 2019) than that of NWA 7680 and NWA 6962.

Although the major element compositions of their olivine ($Fa_{49.6-54.6}$) are similar to that of NWA 7680 and NWA 6962. Tafassasset has olivine compositions distinct from NWA 7680 and NWA 6962 as well ($Fa_{28.6}$, Fe/Mn = 61.9, CaO = 0.05 wt.%; Gardner-Vandy et al. 2012). These compositions suggest a diverse set of melts being generated from CR chondrite-like materials.

A modal recombination was carried out to emulate whole rock REE patterns for NWA 7680 and NWA 6962 (Fig. 15). NWA 7680 is largely sub-chondritic, due to its high Fe-metal content. It also has a positive Eu anomaly because of its plagioclase content. NWA 6962 has a pattern that reflects the abundant phosphate in the sample. Other meteorites considered to be evolved from a CR chondrite-like precursor show considerably different whole rock REE abundances. The basaltic achondrite NWA 2976 has REE concentrations on a similar order of magnitude as NWA 6962, but possesses positive Ce and Eu anomalies (Fig. 15). Similar features are seen in the paired meteorite NWA 011 (Yamaguchi et al. 2002). The paired meteorites NWA 6704 and NWA 6693 have variable REE concentrations between samples, but generally have a relatively flat and sub-chondritic pattern with some relative depletion in HREE often observed (Fig. 15). Tafassasset is also quite variable between samples (Fig. 15). Some samples show lower LREE concentrations relative to HREE and positive Eu anomalies. This is similar to the relative abundances seen in NWA 7680; however, the positive Eu anomaly in NWA7680 is much more pronounced. It is apparent that the bulk REE characterization of these early melt products could result in diverse compositions stemming from the heterogeneous nature of the primitive melts forming and intruding into these environments.

Formation of NWA 7680 and NWA 6962

The partial melt environment that produced NWA 7680 and NWA 6962 can be examined in greater detail by observing the mineralogy and textual evidence of crystallization sequence in these meteorites. In both NWA 7680 and NWA 6962 olivine crystallized first. This was followed by chromite and plagioclase, which crystallized in the interstitial space between olivine grains. Metal and sulfide also crystallized between the already formed olivine grains, with the sulfide in particular, often showing anhedral forms suggesting it crystallized later and faster in the sequence. Both NWA 7680 and NWA 6962 are plagioclase-rich relative to chondrites, suggesting a feldspathic melt pooled in their formation area. NWA 7680 is also Fe-metal-rich, suggesting Fe-rich melts were also being produced on the parent body. The mixing of these partial melt products in the formation environment of NWA 7680 and NWA 6962 are indicative of the degree of differentiation that occurred in the parent body. In a larger terrestrial body, feldspathic and Fe-rich melts would separate through gravity-driven differentiation. Such processes were incomplete on the NWA 7680 and NWA 6962 parent body, resulting in the mixing and pooling of partial melt products. Following the initial crystallization sequence(s), a late-stage melt intruded the region. This melt had the most extensive effect on NWA 6962, in which the late-stage melt re-melted and mixed with primary plagioclase (Fig. 2d-f). Clinopyroxene and merrillite also crystallized from this re-melted mixture along with rare titanian chromite. The late-stage melt was less invasive in NWA 7680, often appearing along

grain boundaries and leaving some of the primary plagioclase crystals intact (Fig. 16). This late-stage melt injection removed and redistributed primary grains (Fig. 16a inset), and produced silica-rich, alkali-deficient nepheline and rare but distinct K-rich regions at the edges of the melt products (Fig. 16b). Clinopyroxene is often found along grain boundaries associated with nepheline and sulfide suggesting they too were formed during this later intrusion.

Identification and Significance of Nepheline

Both NWA 7680 and NWA 6962 contain silica-rich, alkali-deficient nepheline. Raman spectra (Fig. 3) show similarities between nepheline and tridymite. This is consistent with the similarities in structure, with nepheline simply being "stuffed tridymite" (Buerger 1954). The chemistry of the phase confirms that it is silica-rich, alkali-deficient nepheline similar to terrestrial examples (e.g., Dollase and Thomas 1978). Nepheline has been observed in a number of carbonaceous chondrites and is thought to form through aqueous activity and metasomatic processes (e.g., Tomeoka and Itoh 2004; Matsumoto et al. 2014; Matsumoto et al. 2017). However, CR2 carbonaceous chondrite CAIs are devoid of nepheline (Makide et al. 2009) suggesting they did not experience the metasomatic processes experienced by CAIs in CV chondrites (Krot et al. 1998). Carbonaceous chondrite nepheline is similar in composition to that of NWA 7680 and NWA 6962; however, the Si-enrichment in the carbonaceous achondrites generally exceeds that of reported chondritic nepheline. Locating nepheline in ungrouped achondrites could be an initially means of associating them with their carbonaceous precursors. These late nepheline-forming melts may also be a common feature in carbonaceous achondrite forming environments and should be considered when modelling these early melt environments and when analyzing bulk analytical data from these rocks.

Metal Texture, Compositional Variability and the Source of Phosphorus

Etching of the largest metal-rich area in a slab of NWA 7680 revealed polygonal domains, each a few millimeters across (Fig. 1). Neumann bands were observed within the polygonal domains (Fig. 1). These bands form during high pressure events, such as impacts, but temperatures must remain below 600 °C and probably below 300 °C (Uhlig 1955) for them to remain intact. Metal from the polygonal domains as well as some of the metal associated with silicates have homogeneous Co/Ni compositions (Fig. 8). Metal from NWA 6962 also have relatively homogenized Co/Ni compositions. Nickel-rich blebs found within the polygonal domains of NWA 7680 have low Co concentrations relative to primitive solar system values. Some of the metal associated with silicates in NWA 7680 exhibit heterogeneous Co/Ni values; both high Co and low Co compositions are observed.

The metal Co/Ni composition of CR chondrites is generally primitive, although some scatter deviation is evident (Connolly et al. 2001; Krot et al. 2002; Jacquet et al. 2013). This primitive composition is the result of limited or no thermal metamorphism being experienced by the majority of these meteorites. Thermal metamorphism is evident in a few CR chondrites (Abreu and Bullock 2013; Briani et al. 2013). Using these primitive compositions as a starting

point future research could examine the evolution of these metal compositions, including examination of highly siderophile element compositions (Nicklas et al. 2022).

The metal content of these meteorites may also be related to the phosphates present. Phosphates in some chondrites are associated with metal, suggesting P-rich metal was the initial source of phosphorus (e.g., Perron et al. 1992; Zanda et al. 1994; Ward et al. 2017). This is consistent with numerous phosphate grains being associated with metal in NWA 7680 (Fig. 4a and Fig. 4c) and in some cases in NWA 6962. However, the merrillite in NWA 6962 appears to be from a more evolved melt linked to the late-stage intrusion discussed earlier. Some of the merrillite in NWA 6962 has a sponge-like texture (Fig. 4f) possibly due to terrestrial weathering. Terrestrial weathering is also apparent in some of the metal. These potentially weathered phosphate grains were not used for the U-Pb ratio isotopic analyses discussed below.

Timing, Phosphate Closure Temperature and Constraining Disk Reservoir Separation

The weighted mean $^{207}Pb/^{206}Pb$ ages for NWA 7680 and NWA 6962 phosphates overlap within the uncertainties provided. These values also overlap with age data from the basaltic carbonaceous achondrite NWA 2976. Whole-rock and pyroxene Pb-Pb ages (corrected with the measured $^{238}U/^{235}U$) from NWA 2976 (paired with NWA 011) reveal an age of 4562.89 ± 0.59 Ma (Bouvier et al. 2011). This shows that basaltic melts were also being generated on CR chondrite-like parent bodies early in the solar system's history. NWA 6704 and NWA 6693 have pyroxene Pb-isotopic ages (measured $^{238}U/^{235}U$) of 4562.76 ± 0.22/0.30 Ma and 4562.63 ± 0.29/0.21 Ma respectively (Amelin et al. 2019). This adds to the diversity of melts formed on a CR chondrite-like parent body during this period. Recent work on *in situ* dating of merrillite grains in Tafassasset reveals a $^{207}Pb/^{206}Pb$ age of 4548.7±8.1 Ma (Schwarz et al. 2021), which is younger than Pb-Pb model ages reported for fragments (Göpel et al. 2009). The merrillite age is within uncertainty of NWA 6962 phosphate ages, but suggests that thermal and/or impact events were affecting the U-Pb system in phosphates later in the history of Tafassasset's parent body. Further study of these phosphates is necessary to assess the implications of these younger dates in relation to processes on CR chondrite-like parent bodies.

The ages of NWA 7680 and NWA 6962 confirm that they have not experienced any long duration thermal metamorphism, above the closure temperature of the phosphates, since the first several million years of the solar system's formation. For apatite this closure temperature is only 400–600 °C for the smaller grains found in these meteorites, at slow cooling rates (Fig. S1; Dodson 1973; Cherniak et al. 1991; Harrison et al. 2002; Maeda et al. 2011). Application of this temperature range assumes that merrillite has a similar closure temperature to apatite. Apatite and merrillite from NWA 6962 have identical formation ages (within uncertainty), suggesting they have experienced similar thermal pathways since their formation. The phosphate grains in these meteorites also have not experienced impact related Pb loss and age resetting as seen in examples of phosphates from other achondrites (Koike et al. 2020; White et al. 2021), chondrites (Yin et al. 2014; Li and Hsu 2018), and terrestrial impact sites (McGregor et al. 2018). The antiquity of the phosphates in NWA 7680 and NWA 6962 suggests that the textures, mineralogy

and geochemistry observed are the products of early solar system processes and have not been disturbed by subsequent geologic events (e.g., impacts or melt generation). Even the latest-stage melt products, most prevalent in NWA 6962, would have had to crystallize in the first several million years of the solar system.

The age data acquired for NWA 7680 and NWA 6962 provides an opportunity to examine isotopic reservoirs in the solar system's formative years. Oxygen isotope compositions for NWA 7680 and NWA 6962 overlap those of the acapulcoites and lodranites (Fig. 11 and Greenwood et al. 2012) and also fall within the field of ureilite compositions. Past research has suggested that there are subsets within the ureilites based on oxygen isotope compositions, with the largest subset having a $\Delta^{17}O$ of -0.98‰ (Ash et al. 2000; Franchi 2008; Rumble et al. 2010). The ureilite field has since been shown to be a continuum (e.g., Greenwood et al. 2017). However, the large number of ureilites at -0.98‰ $\Delta^{17}O$ could be the result of one of the source materials that have come together to form the ureilite parent body. Additionally, meteorites such as NWA 11119 (Srinivasan et al. 2018) and ALM-A (Almahata Sitta) (Bischoff et al. 2014) also fall in the same region of oxygen isotope space (Fig. 11) and others such as NWA 7325 have similar $\Delta^{17}O$ compositions (Barrat et al. 2015; Weber et al. 2016). However, it has been shown that all of these achondrites originate from the inner solar system (Huyskens et al. 2018; Sanborn et al. 2019; Zhu et al. 2020), whereas NWA 7680 and NWA 6962 originate from the outer solar system along with the CR chondrites. One possible explanation for this is a common reservoir of early accretionary materials with a ~ -1‰ $\Delta^{17}O$ oxygen isotope signature. Such a reservoir would have formed prior to the establishment of the Cr-isotope dichotomy and would have been redistributed into both the inner and outer solar system. Jupiter must have formed prior to the establishment of the observed Cr-isotope dichotomy (Fig. 12). Additionally, the Cr-isotope signature must have been established before the formation of NWA 7680 and NWA 6962. Since NWA 7680 and NWA 6962 phosphates have retained ages from the first several million years of the solar system's formation, it is certain that the observed Cr isotope compositions were not introduced by a later high temperature event, such as a recent impact accretionary process. This is consistent with past work suggesting a rapid Jupiter formation. Kruijer et al. (2017) recently used Mo and W isotope measurements of iron meteorites to observe that the meteorites derive from two distinct reservoirs. They suggest that the separation of these reservoirs was the result of Jupiter's formation, reaching ~20 Earth masses in less than one million years.

CONCLUSIONS

Early solar system melt environments have been preserved in NWA 7680 and NWA 6962. The meteorites have mineralogical and geochemical similarities that confirm they are from the same parent body. The meteorites are plagioclase-rich and NWA 7680 is also Fe-metal-rich, suggesting they both formed through incomplete differentiation processes that resulted in the pooling of partial melt products. The meteorites were formed through partial melting on a CR chondrite-like parent body. Evidence for the intrusion of a late-stage melt is observed in both

meteorites. The late-stage melt products include silica-rich, alkali-deficient nepheline. *In situ* dating of merrillite and fluorapatite reveals that NWA 7680 has remained unaffected by long duration thermal metamorphism and impact resetting since 4578 ± 17 Ma. Phosphates in NWA 6962 also formed early (4556.6 ± 8.0 Ma) and remained unaffected by such events. The thermochronology data proves that the Cr isotope compositions were not introduced by a recent high temperature event, which is consistent with the early establishment of two distinct geochemical reservoirs coinciding with the growth and formation of Jupiter.

ACKNOWLEDGMENTS

This project was funded in part by a National Sciences and Engineering Research Council (NSERC) PGS D and Ontario Graduate Scholarship (OGS) Award to B.C. Hyde and NSERC Discovery Grant to K.T. Tait and D.E. Moser. Travel funding was provided by a Mineralogical Association of Canada Student Travel Grant. Q.-Z. Yin acknowledges NASA EW Grant Support NNX16AD34G. We are grateful to David Gregory for his donation of the NWA 7680 material for this study. We thank the technical team in Laboratory for Stable Isotope Science (LSIS), University of Western Ontario, for help and encouragement with the oxygen isotopic analyses. Funding for the oxygen isotope work was provided by NSERC, the Ontario Centre of Excellence, CFI, and the UWO Academic Development Fund. We also thank Ivan Barker, Ian Nicklin, Veronica Di Cecco, Katherine Dunnell and Brian Joy for technical support during material preparation and analysis. Phil McCausland, Roberta Flemming and Elizabeth Webb are thanked for helpful discussion.

Supporting Information

Additional supporting information may be found in the online version of this article:

Table S1. EPMA Standards (left) used for analysis of sample (top) compositions. Elements standardized from each standard are given in the table.

Table S2. Composition of feldspar in order of increasing An-content. Oxide values are in wt.% and Or-An-Ab values are % in atoms per formula unit.

Table S3. Average CI chondrite normalized rare earth element compositions for minerals in NWA 7680 and 6962.

Supporting Text. Terrestrial basalt compositions (Fig. 13) were downloaded from PetDB (www.earthchem.org/petdb) on 7, July 2020. The search was carried out for basalts. This was then refined to whole rock analyses from spreading centres. Data with unknown methodology were removed and DCP data were also removed as multiple entries for these analyses contained concentrations of 0 wt.% for compositions being plotted.

Figure S1. Calculated closure temperatures for grains in NWA 7680 and NWA 6962 following the methods of Dodson 1973, Cherniak et al. 1991 and Maeda et al. (2011). The calculated temperatures span a range of slow cooling rates. Grain sizes shown are the longest

measured dimension for the largest and smallest phosphate grains analyzed. The 680 μm grain is unusually large with all other grains being less than 400 μm and most being less than 300 μm.

REFERENCES

Abe D., Mikouchi T. and Irving A. J. 2021. Experimental Evidence for Formation of Northwest Africa 6962 CR-Related Achondrite from a CR Chondrite Precursor Melt (abstract #1813). 52nd Lunar and Planetary Science Conference.

Abreu N. M. and Bullock, E. S. 2013. Opaque assemblages in CR2 Graves Nunataks (GRA) 06100 as indicators of shock-driven hydrothermal alteration in the CR chondrite parent body. *Meteoritics & Planetary Science* 48(12):2406-2429

Ali A., Jabeen I., Gregory D., Verish R. and Banerjee N. R. 2016. New triple oxygen isotope data of bulk and separated fractions from SNC meteorites: Evidence for mantle homogeneity of Mars. *Meteoritics & Planetary Science* 51(5):981–995.

Ali A., Jabeen I., Banerjee N. R., Osinski G. R., Nicklin I., Gregory D. and Herrmann P. 2018. The oxygen isotope compositions of olivine in main group (MG) pallasites: New measurements by adopting an improved laser fluorination approach. *Meteoritics & Planetary Science* 53(6):1223–1237.

Amelin Y., Koefoed P., Iizuka T., Fernandes V. A., Huyskens M. H., Yin Q. Z. and Irving A. J. 2019. U-Pb, Rb-Sr and Ar-Ar systematics of the ungrouped achondrites Northwest Africa 6704 and Northwest Africa 6693. *Geochimica et Cosmochimica Acta* 245:628–642.

Ash R. D., MacPherson G. J. and Rumble III D. 2000. Oxygen isotopes, ureilite genesis, and the geology of asteroids (abstract #5288). 63rd Annual Meeting of the Meteoritical Society.

Barrat J. A., Greenwood R. C., Verchovsky A. B., Gillet P., Bollinger, C., Langlade J. A., Liorzou C. and Franchi I. A. 2015. Crustal differentiation in the early solar system: Clues from the unique achondrite Northwest Africa 7325 (NWA 7325). *Geochimica et Cosmochimica Acta* 168:280-292.

Bischoff A., Horstmann M., Barrat J. A., Chaussidon M., Pack A., Herwartz D., Ward D., Vollmer C. and Decker S. 2014. Trachyandesitic volcanism in the early solar system. *Proceedings of the National Academy of Sciences* 111(35):12689–12692.

Bogdanovski O. and Lugmair G. W. 2004. Manganese-chromium isotope systematics of basaltic achondrite Northwest Africa 011 (abstract #1715). 35th Lunar and Planetary Science Conference.

Bourot-Denise M., Zanda B. and Javoy M. 2002. Tafassasset: An equilibrated CR chondrite (abstract #1611). 33rd Lunar and Planetary Science Conference.

Bouvier A., Spivak-Birndorf L. J., Brennecka G. A. and Wadhwa M. 2011. New constraints on early Solar System chronology from Al–Mg and U–Pb isotope systematics in the unique basaltic achondrite Northwest Africa 2976. *Geochimica et Cosmochimica Acta* 75(18):5310–5323.

Briani G., Quirico E., Gounelle M., Paulhiac-Pison M., Montagnac G., Beck, P., Orthous-Daunay F.R., Bonal L., Jacquet E., Kearsley A. and Russell S.S. 2013. Short duration thermal metamorphism in CR chondrites. *Geochimica et Cosmochimica Acta* 122:267–279.

Bridges J. C., Hutchison R., Franchi I. A., Alexander C. M. and Pillinger C. T. 1995. A feldspar-nepheline achondrite clast in Parnalle. *Antarctic Meteorite Research* 8:195–203.

Budde G., Burkhardt C., Brennecka G. A., Fischer-Gödde M., Kruijer T. S. and Kleine T. 2016. Molybdenum isotopic evidence for the origin of chondrules and a distinct genetic heritage of carbonaceous and non-carbonaceous meteorites. *Earth and Planetary Science Letters* 454:293–303.

Buerger M. J. 1954. The stuffed derivatives of the silica structures. *American Mineralogist* 39(7-8):600–614.

Bunch T. E., Irving A. J., Larson T. E., Longstaffe F. J., Rumble III D. and Wittke, J. H. 2005. "Primitive" and igneous achondrites related to the large and differentiated CR parent body (abstract #2308). 36th Lunar and Planetary Science Conference.

Bunch T. E., Irving A. J., Wittke J. H., Rumble D., Gellissen M. and Palme H. 2008. Evidence for pervasive metamorphism on the CR chondrite parent body from highly equilibrated CR6 chondrites Northwest Africa 2994 and Northwest Africa 3100 (abstract #1991). 39th Lunar and Planetary Science Conference.

Cherniak D. J., Lanford W. A. and Ryerson F. J. 1991. Lead diffusion in apatite and zircon using ion implantation and Rutherford Backscattering techniques. *Geochimica et Cosmochimica Acta* 55(6):1663–1673.

Chew D. M., Petrus J. A. and Kamber B. S. 2014. U–Pb LA–ICPMS dating using accessory mineral standards with variable common Pb. *Chemical Geology* 363:185–199.

Clayton R. N. and Mayeda T. K. 1999. Oxygen isotope studies of carbonaceous chondrites. *Geochimica et Cosmochimica Acta* 63(13-14):2089–2104.

Connelly J. N., Bizzarro M., Krot A. N., Nordlund Å., Wielandt D. and Ivanova M. A. 2012. The absolute chronology and thermal processing of solids in the solar protoplanetary disk. *Science* 338:651–655.

Connelly J. N., Schiller M. and Bizzarro M. 2019. Pb isotope evidence for rapid accretion and differentiation of planetary embryos. *Earth and Planetary Science Letters* 525:115722, doi.org/10.1016/j.epsl.2019.115722

Connolly Jr H. C., Huss G. R., and Wasserburg G. J. 2001. On the formation of Fe-Ni metal in Renazzo-like carbonaceous chondrites. *Geochimica et Cosmochimica Acta* 65(24):4567–4588.

Dauphas N., Remusat L., Chen J. H., Roskosz M., Papanastassiou D. A., Stodolna J., Guan Y., Ma C. and Eiler J. M. 2010. Neutron-rich chromium isotope anomalies in supernova nanoparticles. *The Astrophysical Journal*, 720:1577–1591.

Davidson J., Schrader D. L., Alexander C. M. O. D., Lauretta D. S., Busemann H., Franchi I. A., Greenwood R. C., Connolly Jr H. C., Domanik K. J. and Verchovsky A. 2014. Petrography, stable isotope compositions, microRaman spectroscopy, and presolar components of Roberts Massif 04133: A reduced CV3 carbonaceous chondrite. *Meteoritics & Planetary Science* 49(12):2133–2151.

Dodson M. H. 1973. Closure temperature in cooling geochronological and petrological systems. *Contributions to Mineralogy and Petrology* 40(3):259-274.
Dollase W. A. and Thomas W. M. 1978. The crystal chemistry of silica-rich, alkali-deficient nepheline. *Contributions to Mineralogy and Petrology* 66(3):311–318.
Dunlap D. R., Ku Y. J., Garvie L. A. J. and Wadhwa M. 2015. Petrology of Ungrouped and Anomalous Achondrites SaU 493, NWA 4470, NWA 6962, and NWA 5297 (abstract #2570). 46th Lunar and Planetary Science Conference.
Floss C. 2000. Complexities on the acapulcoite-lodranite parent body: Evidence from trace element distributions in silicate minerals. *Meteoritics & Planetary Science* 35(5):1073–1085.
Floss C., Taylor L.A., Promprated P. and Rumble III D. 2005. Northwest Africa 011: A "eucritic" basalt from a non-eucrite parent body. *Meteoritics & Planetary Science* 40(3):343–360.
Franchi I. A. 2008. Oxygen isotopes in asteroidal materials. In *Reviews in Mineralogy and Geochemistry*, *68*(1), edited by MacPherson G. J., Mittlefehldt D. W., Jones J. H. and Simon S. B. Virginia: Mineralogical Society of America. pp. 345–397.
Gardner-Vandy K. G., Lauretta D. S., Greenwood R. C., McCoy T. J., Killgore M. and Franchi I. A. 2012. The Tafassasset primitive achondrite: Insights into initial stages of planetary differentiation. *Geochimica et Cosmochimica Acta* 85:142–159.
Goodrich C. A. and Righter K. 2000. Petrology of unique achondrite Queen Alexandra Range 93148: A piece of the pallasite (howardite-eucrite-diogenite?) parent body? *Meteoritics & Planetary Science* 35(3):521–535.
Goodrich C. A., Kita N. T., Spicuzza M. J., Valley J. W., Zipfel J., Mikouchi T., and Miyamoto M. 2010. The Northwest Africa 1500 meteorite: Not a ureilite, maybe a brachinite. *Meteoritics & Planetary Science* 45(12):1906-1928.
Göpel C., Birck J. L. and Manhès G. 2009. U/Pb and Cr isotope study of the Tafassasset meteorite (abstract #5267). 72nd Annual Meeting of the Meteoritical Society.
Göpel C., Birck J. L., Galy A., Barrat J. A., and Zanda B. 2015. Mn–Cr systematics in primitive meteorites: Insights from mineral separation and partial dissolution. *Geochimica et Cosmochimica Acta* 156:1-24.
Greenwood R. C., Franchi I. A., Gibson J. M. and Benedix G. K. 2012. Oxygen isotope variation in primitive achondrites: The influence of primordial, asteroidal and terrestrial processes. *Geochimica et Cosmochimica Acta* 94:146–163.
Greenwood R. C., Burbine T. H., Miller M. F. and Franchi I. A. 2017. Melting and differentiation of early-formed asteroids: The perspective from high precision oxygen isotope studies. *Chemie der Erde* 77(1):1–43.
Guan Y. and Crozaz G. 2000. Light rare earth element enrichments in ureilites: a detailed ion microprobe study. *Meteoritics & Planetary Science* 35(1):131–144.
Guan Y. and Crozaz G. 2001. Microdistributions and petrogenetic implications of rare earth elements in polymict ureilites. *Meteoritics & Planetary Science* 36(8):1039–1056.
Guillong M., Meier D. L., Allan M. M., Heinrich C. A. and Yardley B. W. 2008. Appendix A6: SILLS: A MATLAB-based program for the reduction of laser ablation ICP-MS data of

homogeneous materials and inclusions. In *Mineralogical Association of Canada Short Course*, *40*, edited by Sylvester, P. Vancouver: Mineralogical Association of Canada. pp. 328–333.

Harrison T. M., Catlos E. J. and Montel J. M. 2002. U-Th-Pb dating of phosphate minerals. In *Reviews in Mineralogy and Geochemistry* 48(1), edited by Kohn M. J., Rakovan J., Hughes J. M. Virginia: Mineralogical Society of America. pp. 524–558.

Hibiya Y., Archer G. J., Tanaka R., Sanborn M. E., Sato Y., Iizuka T., Ozawa K., Walker R. J., Yamaguchi A., Yin Q. Z. and Nakamura T. 2019. The origin of the unique achondrite Northwest Africa 6704: Constraints from petrology, chemistry and Re–Os, O and Ti isotope systematics. *Geochimica et Cosmochimica Acta* 245:597–627.

Huyskens M. H., Sanborn M. E., Yin Q. Z. and Agee C. B. 2018. Silica-rich magmatism in the early solar system: U-Pb and Al-Mg chronology and Cr isotopes of ungrouped achondrite Northwest Africa 11119 (abstract #2311). 49th Lunar and Planetary Science Conference.

Irving A. J., Kuehner S. M. and Ziegler, K. 2013. Petrology and oxygen isotopic composition of brachinite-like achondrites Northwest Africa 7388 and Northwest Africa 7605, and evidence for late-stage methane-triggered reduction (abstract #2192). 44th Lunar and Planetary Science Conference.

Ivanova M. A. and Petaev M. I. 2015. Characteristics and origin of the components of the carbonaceous chondrite NWA 470. *Petrology* 23(2):150–167.

Jacquet E., Alard O. and Gounelle M. 2012. Chondrule trace element geochemistry at the mineral scale. *Meteoritics & Planetary Science* 47(11):1695–1714.

Jacquet E., Paulhiac-Pison M., Alard O., Kearsley A. T. and Gounelle M. 2013. Trace element geochemistry of CR chondrite metal. *Meteoritics & Planetary Science* 48(10):1981–1999.

Jagoutz E., Palme H., Baddenhausen H., Blum K., Cendales M., Dreibus G., Spettel B., Lorenz V. and Wänke H. 1979. The abundances of major, minor and trace elements in the earth's mantle as derived from primitive ultramafic nodules (abstract). 10th Lunar and Planetary Science Conference 2031–2050.

Jarosewich E. 1990. Chemical analyses of meteorites: A compilation of stony and iron meteorite analyses. *Meteoritics* 25(4):323 –337.

Jogo K., Nagashima, K., Hutcheon I. D., Krot A. N. and Nakamura T. 2013. Heavily metamorphosed clasts from the CV chondrite breccias Mokoia and Yamato-86009. *Meteoritics & Planetary Science* 47(12):2251–2268.

Koike M., Sano Y., Takahata N., Iizuka T., Ono, H. and Mikouchi T. 2020. Evidence for early asteroidal collisions prior to 4.15 Ga from basaltic eucrite phosphate U–Pb chronology. *Earth and Planetary Science Letters* 549:116497.

Krot A. N., Petaev M. I., Scott E. R., Choi B. G., Zolensky M. E. and Keil K. 1998. Progressive alteration in CV3 chondrites: More evidence for asteroidal alteration. *Meteoritics & Planetary Science* 33(5):1065–1085.

Krot A. N., Meibom A., Weisberg M. K. and Keil K. 2002. The CR chondrite clan: Implications for early solar system processes. *Meteoritics & Planetary Science* 37(11):1451–1490.

Kruijer T. S., Burkhardt C., Budde G. and Kleine T. 2017. Age of Jupiter inferred from the distinct genetics and formation times of meteorites. *Proceedings of the National Academy of Sciences* 114(26):6712–6716.

Lafuente B., Downs R. T., Yang H. and Stone N. 2016. The power of databases: The RRUFF project. In *Highlights in Mineralogical Crystallography*, edited by Armbruster T. and Danisi R. M. Berlin: Walter de Gruyter. pp. 1–29.

Leya I., Schönbächler M., Wiechert U., Krähenbühl U. and Halliday A.N. 2008. Titanium isotopes and the radial heterogeneity of the solar system. *Earth and Planetary Science Letters* 266:233–244.

Li S. and Hsu W. 2018. The nature of the L chondrite parent body's disruption as deduced from high-pressure phases in the Sixiangkou L6 chondrite. *Meteoritics & Planetary Science*, 53(10):2107–2122.

Maeda J., Zeniya R., Kuramoto Y., Itaya T. and Kagami H. 2011. A procedure for calculating a consistent set of closure temperatures and cooling rate using Dodson's formula. *The Journal of the Geological Society of Japan* 117(2):99–103.

Makide K., Nagashima K., Krot A. N., Huss G. R., Hutcheon I. D. and Bischoff A. 2009. Oxygen-and magnesium-isotope compositions of calcium–aluminum-rich inclusions from CR2 carbonaceous chondrites. *Geochimica et Cosmochimica Acta* 73(17):5018–5050.

Matsumoto M., Tomeoka K., Seto Y., Miyake A. and Sugita M. 2014. Nepheline and sodalite in the matrix of the Ningqiang carbonaceous chondrite: Implications for formation through parent-body processes. *Geochimica et Cosmochimica Acta* 126:441–454.

Matsumoto M., Tomeoka K. and Seto Y. 2017. Nepheline and sodalite in chondrules of the Ningqiang carbonaceous chondrite: Implications for a genetic relationship with those in the matrix. *Geochimica et Cosmochimica Acta* 208:220–233.

McDonough W. F. and Sun S.-S. 1995. The composition of the Earth. *Chemical Geology* 120:223–253.

McDowell F. W., McIntosh W. C. and Farley K. A. 2005. A precise ^{40}Ar–^{39}Ar reference age for the Durango apatite (U–Th)/He and fission-track dating standard. *Chemical Geology* 214(3-4):249–263.

McGregor M., McFarlane C. R. and Spray J. G. 2018. In situ LA-ICP-MS apatite and zircon U–Pb geochronology of the Nicholson Lake impact structure, Canada: shock and related thermal effects. *Earth and Planetary Science Letters* 504:185-197.

Mittlefehldt D. W., McCoy T. J., Goodrich C. A. and Kracher, A. 1998. Non-chondritic meteorites from asteroidal bodies. In *Planetary Materials, Reviews in Mineralogy and Geochemistry* 36, edited by Papike J. J. Washington: Mineralogical Society of America. pp. 4-1–4-195.

Nanne J. A., Nimmo F., Cuzzi J. N. and Kleine T. 2019. Origin of the non-carbonaceous-carbonaceous meteorite dichotomy. *Earth and Planetary Science Letters* 511:44–54.

Nicklas R. W., Day J. M. D., Vaci Z. and Ren M. 2022. Brachinite highly siderophile element systematics indicate retention of a Pt-rich phase during chondrite melting (abstract #1018). 53rd Lunar and Planetary Science Conference.

Perron C., Bourot-Denise M., Marti K., Kim J. S. and Crozaz G. 1992. The metal-phosphate connection in chondrites. *Meteoritics* 27(3):275.

Qin L., Nittler L. R., Alexander C. O. D., Wang J., Stadermann F. J. and Carlson R. W. 2011. Extreme ^{54}Cr-rich nano-oxides in the CI chondrite Orgueil - Implication for a late supernova injection into the solar system. *Geochimica et Cosmochimica Acta* 75:629–644.

Righter K., Drake M. J. and Scott E. 2006. Compositional relationships between meteorites and terrestrial planets. In *Meteorites and the early solar system II*, edited by Lauretta D. S. and McSween H. Y. Arizona: University of Arizona Press. pp. 803–828.

Rumble D., Zolensky M. E., Friedrich J. M., Jenniskens P. and Shaddad M. H. 2010. The oxygen isotope composition of Almahata Sitta. *Meteoritics & Planetary Science* 45(10-11):1765–1770.

Ruzicka A., Grossman J., Bouvier A., Herd C. D. K. and Agee C. B. 2015a. The Meteoritical Bulletin, No. 102. *Meteoritics & Planetary Science* 50:1662.

Ruzicka A., Grossman J., Bouvier A., Herd C. D. K. and Agee C. B. 2015b. The Meteoritical Bulletin, No 101. *Meteoritics & Planetary Science* 50:1661.

Sanborn M. E. and Yin Q. Z. 2019. Magmatism in the outer solar system: What we know now from isotope forensics of carbonaceous achondrites (abstract #1498). 50th Lunar and Planetary Science Conference.

Sanborn M. E., Yamakawa A., Yin Q. Z., Irving A. J. and Amelin Y. 2013. Chromium isotopic studies of ungrouped achondrites NWA 7325, NWA 2976, and NWA 6704 (abstract #5220). 76th Annual Meeting of the Meteoritical Society.

Sanborn M. E., Wimpenny J., Williams C. D., Yamakawa A., Amelin Y., Irving A. J., and Yin Q. Z. 2019. Carbonaceous achondrites Northwest Africa 6704/6693: Milestones for early Solar System chronology and genealogy. *Geochimica et Cosmochimica Acta* 245:577–596.

Schrader D. L., Davidson J., Greenwood R. C., Franchi I. A., and Gibson J. M. 2014. A water–ice rich minor body from the early Solar System: The CR chondrite parent asteroid. *Earth and Planetary Science Letters* 407:48-60.

Schwarz W. H., Hopp J., Ludwig T., Bouvier A., Trieloff M., Ma N., Gail H. P. and Neumann W. 2021. Pb-Pb Ages of Chondritic Phosphates (abstract #1981). 52nd Lunar and Planetary Science Conference.

Shields W. R., Murphy T. J., Catanzaro E. J., and Garner E. L. 1966. Absolute isotopic abundance ratios and the atomic weight of a reference sample of chromium. *Journal of Research of the National Bureau of Standard* 70A:193-197.

Srinivasan P., Dunlap D. R., Agee C. B., Wadhwa M., Coleff D., Ziegler K., Zeigler R. and McCubbin F. M. 2018. Silica-rich volcanism in the early solar system dated at 4.565 Ga. *Nature Communications* 9, 3036, doi:10.1038/s41467-018-05501-0

Thomson S. N., Gehrels G. E., Ruiz J. and Buchwaldt R. 2012. Routine low-damage apatite U-Pb dating using laser ablation–multicollector–ICPMS. *Geochemistry, Geophysics, Geosystems*, *13*(2):Q03017.

Tomeoka K. and Itoh D. 2004. Sodium-metasomatism in chondrules in CO3 chondrites: Relationship to parent body thermal metamorphism. *Meteoritics & Planetary Science* 39(8):1359–1373.

Trinquier A., Birck J.-L., and Allegre C. J. 2007. Widespread ^{54}Cr heterogeneity in the inner solar system. *The Astrophysical Journal* 655:1179 –1185.

Trinquier A., Elliott T., Ulfbeck D., Coath C., Krot A. N. and Bizzarro, M. 2009. Origin of nucleosynthetic isotope heterogeneity in the solar protoplanetary disk. *Science* 324(5925):374–376.

Uhlig H.H. 1955. Contribution of metallurgy to the origin of meteorites Part II–the significance of Neumann bands in meteorites. *Geochimica et Cosmochimica Acta* 7(1-2):34–42.

Valley J. W., Kitchen N., Kohn M. J., Niendorf C. R. and Spicuzza M. J. 1995. UWG-2, a garnet standard for oxygen isotope ratios: strategies for high precision and accuracy with laser heating. *Geochimica et Cosmochimica Acta* 59(24):5223–5231.

Ward D., Bischoff A., Roszjar J., Berndt J. and Whitehouse M. J. 2017. Trace element inventory of meteoritic Ca-phosphates. *American Mineralogist* 102(9):1856–1880.

Warren P. H. 2011. Stable-isotopic anomalies and the accretionary assemblage of the Earth and Mars: A subordinate role for carbonaceous chondrites. *Earth and Planetary Science Letters* 311: 93–100.

Warren P. H., Rubin A. E., Isa J., Brittenham S., Ahn I. and Choi B. G. 2013. Northwest Africa 6693: A new type of FeO-rich, low-Δ^{17}O, poikilitic cumulate achondrite. *Geochimica et Cosmochimica Acta* 107:135–154.

Weber I., Morlok A., Bischoff A., Hiesinger H., Ward D., Joy K. H., Crowther S. A., Jastrzebski N. D., Gilmour J. D., Clay P. L. Wogelius, R.A., Greenwood R. C., Franchi I. A. and Münker C. 2016. Cosmochemical and spectroscopic properties of Northwest Africa 7325 - A consortium study. *Meteoritics & Planetary Science* 51(1):3-30.

Weisberg M. K., Prinz M., Clayton R. N. and Mayeda T. K. 1993. The CR (Renazzo-type) carbonaceous chondrite group and its implications. *Geochimica et Cosmochimica Acta* 57(7):1567–1586.

White L. F., Moser D. E., Darling J. R., Rider-Stokes B., Hyde B., Tait K. T., Chamberlain K. and Schmitt A. K. 2021. Accessory Mineral Chronology of Eucrites Reveals New Insights into the Formation, Evolution, and Bombardment of Vesta. (abstract # 2124) 52nd Lunar and Planetary Science Conference.

Wimpenny J., Sanborn M. E., Koefoed P., Cooke I. R., Stirling C., Amelin Y. and Yin Q.-Z. 2019. Reassessing the origin and chronology of the unique achondrite Asuka 881394: Implications for distribution of ^{26}Al in the early Solar System. *Geochimica et Cosmochimica Acta* 244:478–501.

Yamakawa A., Yamashita K., Makishima A., and Nakamura E. 2009. Chemical separation and mass spectrometry of Cr, Fe, Ni, Zn, and Cu in terrestrial and extraterrestrial materials using thermal ionization mass spectrometry. *Analytical Chemistry* 81:9787-9794.

Yamaguchi A., Clayton R. N., Mayeda T. K., Ebihara M., Oura Y., Miura Y. N., Haramura H., Misawa K., Kojima H. and Nagao K. 2002. A new source of basaltic meteorites inferred from Northwest Africa 011. *Science* 296(5566):334–336.

Yin Q., Jacobsen S. B. and Yamashita K. 2002. Diverse supernova sources of pre-solar material inferred from molybdenum isotopes in meteorites. *Nature* 415:881–883.

Yin Q. Z., Zhou Q., Li Q. L., Li X. H., Liu Y., Tang G. Q., Krot A. N. and Jenniskens P. 2014. Records of the Moon-forming impact and the 470 Ma disruption of the L chondrite parent body in the asteroid belt from U-Pb apatite ages of Novato (L6). *Meteoritics & Planetary Science* 49(8):1426–1439.

Zanda B., Bourot-Denise M., Perron C. and Hewins R. H. 1994. Origin and metamorphic redistribution of silicon, chromium, and phosphorus in the metal of chondrites. *Science* 265(5180):1846-1849.

Zhang A., Guan Y., Hsu, W., Liu Y. and Taylor L.A. 2010. Origin of a metamorphosed lithic clast in CM chondrite Grove Mountains 021536. *Meteoritics & Planetary Science* 45(2):238–245.

Zhu K., Moynier F., Schiller M., Wielandt D., Larsen K. K., van Kooten E. M., Barrat J. A. and Bizzarro M. 2020. Chromium isotopic constraints on the origin of the ureilite parent body. *The Astrophysical Journal* 888(2):126.

TABLES

Table 1. Average (±1σ) mineral compositions (wt.%) for NWA 7680. Italicized values are in element % (not oxide %). When compositions are below detection limits the concentrations are noted as less than the 3σ lower limit of detection. The highest calculated 3σ value for a single point is given.

NWA 7680	olivine	clinopyroxene	nepheline	merrillite	fluorapatite	chromite	metal	sulfide	
	n=72	*n=42*	*n=17*	*n=26*	*n=10*	*n=35*	*n=246*	*n=52*	
SiO_2	34.96±0.17	53.20±0.59	49.30±1.12	0.11±0.03	0.21±0.06	0.04±0.02	*<0.04*	*<0.04*	*Si*
P_2O_5	-	-	-	45.99±0.45	41.52±0.19	-	*<0.02*	*<0.02*	*P*
Na_2O	<0.04	0.71±0.15	16.17±0.17	2.76±0.09	0.29±0.03	-	-	-	*Na*
MgO	26.48±0.16	13.33±0.99	0.07±0.01	3.04±0.10	0.02±0.01	3.46±0.84	-	-	*Mg*

Al_2O_3	<0.03	0.91±0.19	30.71±0.59	<0.02	<0.02	12.67±3.29	-	-	*Al*
K_2O	<0.04	<0.02	2.95±0.45	0.09±0.03	<0.02	-	-	-	*K*
CaO	0.47±0.05	22.67±0.45	0.36±0.07	46.50±0.32	54.05±0.19	-	-	-	*Ca*
TiO_2	<0.06	0.30±0.20	<0.01	-	-	3.09±1.29	-	-	*Ti*
V_2O_3	<0.07	<0.05	-	-	-	0.74±0.05	-	-	*V*
Cr_2O_3	0.02±0.03	0.91±0.32	-	-	-	46.27±1.25	-	-	*Cr*
MnO	0.52±0.02	0.11±0.02	-	0.03±0.02	<0.04	0.39±0.03	-	-	*Mn*
FeO	38.26±0.24	8.04±1.36	0.39±0.13	1.41±0.27	0.79±0.23	30.94±1.81	*90.22±8.07*	*63.29±0.33*	*Fe*
Fe_2O_3	-	-	-	-	-	1.66±0.41			
CoO	<0.02	<0.04	-	-	-	0.03±0.03	*0.50±0.17*	*<0.03*	*Co*
NiO	<0.1	<0.04	-	-	-	<0.05	*8.98±7.92*	*<0.05*	*Ni*
	-	-	-	-	-	-	-	*36.46±0.20*	*S*
	-	-	-	-	3.61±0.10	-	-	-	*F*
	-	-	-	-	<0.01	-	-	-	*Cl*
					-1.52				*O = F*
									O = Cl
Total	100.71	100.18	99.95	99.93	98.97	99.29	99.7	99.75	

Table 2. Average (±1σ) mineral compositions (wt.%) for NWA 6962. Italicized values are in element % (not oxide %). When compositions are below detection limits the concentrations are noted as less than the 3σ lower limit of detection. The highest calculated 3σ value for a single point is given.

NWA 6962	olivine *n=45*	clinopyroxene *n=75*	nepheline *n=26*	merrillite *n=22*	fluorapatite *n=22*	chromite *n=37*	metal *n=17*	sulfide *n=29*	
SiO_2	35.04±0.20	52.07±1.05	48.58±1.32	0.13±0.03	0.20±0.09	0.05±0.02	<0.04	*0.02±0.02*	*Si*
P_2O_5	-	-	-	46.40±0.51	41.76±0.28	-	<0.02	<0.02	*P*
Na_2O	<0.09	1.01±1.27	17.16±0.28	2.85±0.05	0.08±0.03	-	-	-	*Na*
MgO	24.69±0.20	12.38±1.29	0.15±0.07	3.16±0.08	0.03±0.01	3.74±0.85	-	-	*Mg*
Al_2O_3	<0.06	1.81±2.25	31.16±0.86	<0.02	<0.02	14.38±4.04	-	-	*Al*

K_2O	<0.02	<0.02	2.95±0.33	0.04±0.01	<0.02	-	-	-	*K*
CaO	0.43±0.06	21.35±1.67	0.05±0.04	46.77±0.26	55.04±0.34	-	-	-	*Ca*
TiO_2	<0.04	0.84±0.31	<0.01	-	-	3.51±2.59	-	-	*Ti*
V_2O_3	<0.04	<0.05	-	-	-	0.70±0.04	-	-	*V*
Cr_2O_3	0.02±0.03	0.80±0.26	-	-	-	43.70±1.20	-	-	*Cr*
MnO	0.54±0.02	0.19±0.05	-	0.02±0.02	<0.04	0.37±0.04	-	-	*Mn*
FeO	39.67±0.28	9.67±2.10	0.51±0.15	1.02±0.18	0.31±0.20	31.27±2.88	*98.76±1.70*	*63.63±0.27*	*Fe*
Fe_2O_3	-	-	-	-	-	1.78±0.34			
CoO	<0.04	<0.04	-	-	-	<0.05	*0.23±0.10*	*<0.03*	*Co*
NiO	<0.04	<0.04	-	-	-	<0.05	*2.31±1.72*	*<0.05*	*Ni*
	-	-		-	-	-	-	*36.56±0.17*	*S*
	-	-	-	-	3.99±0.28	-	-	-	*F*
	-	-	-	-	0.40±0.20	-	-	-	*Cl*
					-1.68				*O = F*
					-0.09				*O = Cl*
Total	100.39	100.12	100.56	100.39	100.04	99.5	101.3	100.21	

Table 3. *In situ* spot analyses of U-Pb from phosphates in NWA 7680 and 6962.

1
2
3

FIGURE CAPTIONS

						Data for Tera-Wasserburg plot								Date (Ma)			
	^{206}Pb (cps)	^{238}U (cps)	$\frac{Th}{U}$	$\frac{^{206}Pb}{^{204}Pb}$	2σ	$\frac{^{238}U}{^{206}Pb}$	2σ	$\frac{^{207}Pb}{^{206}Pb}$	2σ	$\frac{^{208}Pb}{^{206}Pb}$	2σ	$\frac{^{208}Pb}{^{232}Th}$	2σ	$\frac{^{207}Pb}{^{206}Pb}$	2σ	$\frac{^{206}Pb}{^{238}U}$	2σ
NWA 7680																	
Section 3 Merrillite 1a	1820	2167	10.3	48	25	0.8961	0.0474	0.6140	0.0220	2.6455	0.0980	0.2548	0.0086	4541	52	4832	255
Section 3 Merrillite 1b	1590	1946	11.3	194	99	0.9141	0.0476	0.6510	0.0250	3.0211	0.1095	0.264	0.0086	4626	55	4764	248
Section 3 Merrillite 1c	1852	2331	9.4	1817	931	0.9372	0.0501	0.6300	0.0230	2.6385	0.0975	0.2663	0.009	4579	53	4681	250
Section 3 Merrillite 1d	1818	2228	8.7	1783	906	0.9066	0.0469	0.6360	0.0240	2.2523	0.0812	0.2559	0.0087	4592	55	4792	248
Section 3 Merrillite 1e	1783	2249	9.2	103	52	0.9217	0.0467	0.6240	0.0210	2.4631	0.0789	0.2556	0.0069	4565	49	4737	240
Section 3 Merrillite 1f	1308	1674	12.3	159	81	0.9311	0.0529	0.6200	0.0220	3.3670	0.1247	0.2554	0.0071	4556	51	4703	267
Section 3 Merrillite 2	1290	1560	13.9	43	22	0.8881	0.0489	0.6480	0.0250	3.6765	0.1352	0.2599	0.0074	4620	56	4862	268
Section 3 Merrillite 3	977	1235	15.5	47	24	0.9328	0.0557	0.6610	0.0300	4.2918	0.2026	0.2586	0.0075	4648	65	4696	280
Section 3 Merrillite 3b	867	1017	14.7	832	424	0.8150	0.0551	0.6300	0.0320	3.8168	0.1748	0.2703	0.0087	4579	74	5161	349
Section 1 Merrillite 8	3160	3970	20.0	104	53	1.0965	0.0385	0.6250	0.0160	5.6561	0.1312	0.2359	0.0057	4567	37	4178	147
Section 1 Fluorapatite 3	3280	4200	1.1	33	17	0.8621	0.0966	0.6450	0.0710	0.2564	0.0920	0.291	0.068	4613	159	4964	556
Merrillite average (n=5) U(ppm) = 0.40±0.11, Th(ppm) = 5.14±0.71																	
NWA 6962																	
Merrillite 3	5650	7480	4.9	510	259	0.9737	0.0370	0.6270	0.0120	1.3550	0.0312	0.2514	0.006	4572	28	4555	173
Merrillite 5	5131	6440	4.2	131	66	0.9242	0.0359	0.6230	0.0120	1.1792	0.0264	0.2698	0.0064	4563	28	4727	184
Merrillite 6	5931	7710	5.3	113	57	0.9569	0.0357	0.6270	0.0120	1.4535	0.0275	0.2538	0.005	4572	28	4612	172
Merrillite 23	6610	8430	3.8	146	74	0.9533	0.0364	0.6190	0.0100	1.0288	0.0349	0.2559	0.0064	4553	23	4624	176
Fluorapatite 1	10880	14620	2.3	241	123	1.0010	0.0341	0.6186	0.0090	0.6068	0.0125	0.2357	0.0056	4552	21	4465	152
Fluorapatite 1b	18960	25890	1.5	485	246	1.0091	0.0336	0.6199	0.0068	0.4114	0.0080	0.2357	0.0052	4555	16	4439	148
Fluorapatite 1c	12860	17120	1.9	458	232	0.9843	0.0339	0.6169	0.0076	0.5408	0.0108	0.2544	0.0061	4548	18	4520	156
Merrillite average (n=2) U(ppm) = 1.84±0.24, Th(ppm) = 9.59±1.76, *Fluorapatite (n=4) U(ppm) = 4.35±1.03, Th(ppm)=8.96±0.80*																	

Figure 1. a) A polished and etched surface of NWA 7680 revealing polygonal Fe-metal grains and silicate-rich region. b) Backscatter electron image of polygonal metal grains showing Neumann bands.

Figure 2. a-c) BSE images of common textures and mineral associations seen in the silicate-rich portion of NWA 7680. d-f) Textures and mineral associations from NWA 6962. Mineral short forms are as follows: olivine (ol), plagioclase (pl), chromite (chr), nepheline (ne), sulfide (s), Fe-metal (m), pyroxene (px), merrillite (mer).

Figure 3. Raman spectra of the Na-rich silicate, nepheline (RRUFF Raman database) and tridymite (RRUFF Raman database).

Figure 4. a-c) BSE images of phosphate minerals and associations seen in NWA 7680. d-f) Phosphate minerals and associations from NWA 6962. Mineral short forms are as follows: fluorapatite (ap), merrillite (mer), olivine (ol), plagioclase (pl), nepheline (ne), sulfide (s), Fe-metal (m), pyroxene (px).

Figure 5. Clinopyroxene (top) and olivine (bottom) major element compositions for NWA 7680 and NWA 6962. Mineral short forms are as follows: diopside (Di), hedenbergite (Hd), enstatite (En), ferrosilite (Fs), forsterite (Fo), fayalite (Fa). Ranges of compositions for ureilites, acapulcoites and lodranites are also shown from Goodrich et al. (2011) and references therein.

Figure 6. CaO and Cr_2O_3 content of olivine in NWA 7680 and NWA 6962 for comparison with acapulcoites-lodranites and ureilites (Goodrich and Righter 2000 and references therein), a Grove Mountains 021536 clast (Zhang et al. 2010) and clasts in Mokoia and Yamato-86009 (Jogo et al. 2013).

Figure 7. Feldspar major element compositions for NWA 7680 and NWA 6962.

Figure 8. Co and Ni concentrations for metal components in NWA 7680 and NWA 6962. The solid line represents the primitive solar ratio (e.g., Davidson et al. 2014).

Figure 9. Rare earth element compositions for a) Phosphates and plagioclase, b) NWA 7680 pyroxene and olivine, and c) NWA 6962 pyroxene and olivine. Note in a) compositions from the feldspar-nepheline (FELINE) clast found in the Parnallee LL 3.6 chondrite are also shown (Bridges et al. 1995). In c) data that are not uniform grey are pyroxene grains formed as replacement of olivine (See Figure 2d). CI chondrite normalization values from McDonough and Sun (1995).

Figure 10. Oxygen isotope values for NWA 7680 bulk powders and grains compared to other carbonaceous achondrites and relevant carbonaceous chondrite trends. Compositions are shown from NWA 6962, NWA 6704, NWA 6693, NWA 011 and Tafassasset (Floss et al. 2005; Gardner-Vandy et al. 2012; Irving et al. 2013; Warren et al. 2013; Hibiya et al. 2019). The carbonaceous chondrite anhydrous mineral (CCAM) line is drawn from data in Clayton and Mayeda (1999) and the CR chondrite trend is a best fit line from the data of Schrader et al. (2014) and references therein. Unless indicated, the 2 SE values are within the areas of the symbols.

Figure 11. Average oxygen isotope values for NWA 7680 bulk powders and grains. Compositions for the achondrites NWA 6962 (Irving et al. 2013), NWA 11119 (Srinivasan et al. 2018), ALMA-A (Bischoff et al. 2014), ureilites (Rumble et al. 2010) and acapulcoites/lodranites (Greenwood et al. 2012) are shown for comparison. Error bars represent 2 SE and *n* denotes the number of analyses.

Figure 12. $\varepsilon^{54}Cr$ vs. $\Delta^{17}O$ diagram showing whole rock NWA 7680 and NWA 6962 compositions in comparison to other achondrite and chondrite meteorites. Literature data are from Sanborn et al. (2019) and references therein. $\Delta^{17}O$ data for NWA 6962 from Irving et al. (2013). The plot shows two distinct groupings: the carbonaceous chondrite-like materials (CC) and the non-carbonaceous materials (NC).

Figure 13. Tera-Wasserburg plots of phosphate data from a) NWA 7680 and c) NWA 6962. Corresponding data used for weighted mean ^{207}Pb-^{206}Pb age shown in b) NWA 7680 and d)

NWA 6962. Red data is from merrillite and blue data is from fluorapatite. All uncertainties are 2σ.

Figure 14. Plot of modal recombination compositions for NWA 7680 and NWA 6962. A dotted trend line is drawn through CR chondrite data, NWA 7680 and NWA 6962. An arrow indicates the direction where fractionation would lead to a roughly basaltic melt composition. CH chondrite and CR chondrite data taken from Ivanova and Petaev (2015) and Weisberg et al. (1993) and references therein. Compositions from the carbonaceous achondrites NWA 6704, NWA 6693 and NWA 011 are taken from Hibiya et al. (2019), Warren et al. (2013) and Yamaguchi et al. (2002) respectively. Ureilite, lodranite-acapulcoite and brachinite compositions are given for comparison (Jarosewich, 1990 and references therein; Mittlefehldt et al. 1998 and references therein). The cosmochemical trend line (through chondritic compositions) and the terrestrial fractionation line are modified from Jagoutz et al. (1979) and Righter et al. (2006) and references therein. Terrestrial basalt compositions were downloaded from PetDB (www.earthchem.org/petdb) on 7, July 2020. The parameters used to acquire the data are found in the Supporting Information online.

Figure 15. Rare earth element patterns calculated from modal recombinations of constituent minerals (whole rock equivalent) in NWA 7680 and NWA 6962. These compositions are compared with NWA 2976 (Bouvier et al. 2011), NWA 6704 and NWA 6963 (Hibiya et al. 2019) and Tafassasset (Gardner-Vandy et al. 2012; Göpel et al. 2015). CI chondrite normalization values are taken from McDonough and Sun (1995).

Figure 16. a) BSE image of NWA 7680 showing late-stage melt intrusion between two large plagioclase crystals and two large olivine crystals. Inset image shows close-up of merrillite grain that has been broken off of surrounding olivine during the melt intrusion. b) Chemical map of the same region highlighting Mg (green), Na (purple), P (yellow) and K (blue). c) RGB-UV CL image showing primary structure in the large plagioclase grains, new growth along edges and mottled melt intrusion.

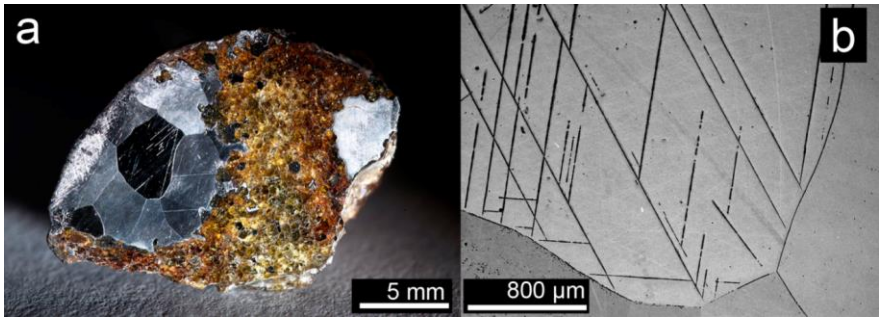

Figure 1. a) A polished and etched surface of NWA 7680 revealing polygonal Fe-metal grains and silicate-rich region. b) Backscatter electron image of polygonal metal grains showing Neumann bands.

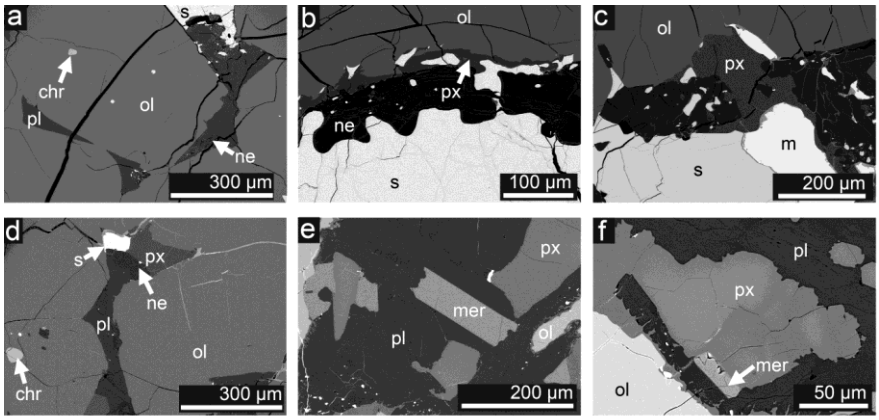

Figure 2. a-c) BSE images of common textures and mineral associations seen in the silicate-rich portion of NWA 7680. d-f) Textures and mineral associations from NWA 6962. Mineral short forms are as follows: olivine (ol), plagioclase (pl), chromite (chr), nepheline (ne), sulfide (s), Fe-metal (m), pyroxene (px), merrillite (mer).

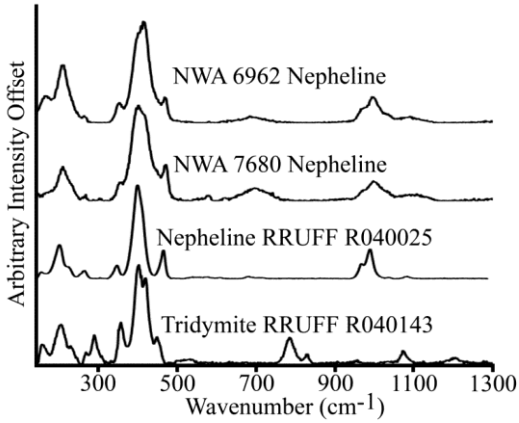

Figure 3. Raman spectra of the Na-rich silicate, nepheline (RRUFF) and tridymite (RRUFF).

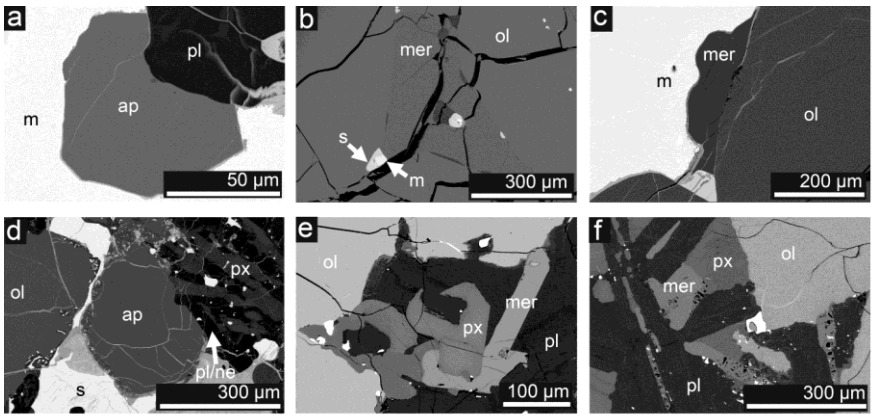

Figure 4. a-c) BSE images of phosphate minerals and associations seen in NWA 7680. d-f) Phosphate minerals and associations from NWA 6962. Mineral short forms are as follows: fluorapatite (ap), merrillite (mer), olivine (ol), plagioclase (pl), nepheline (ne), sulfide (s), Fe-metal (m), pyroxene (px).

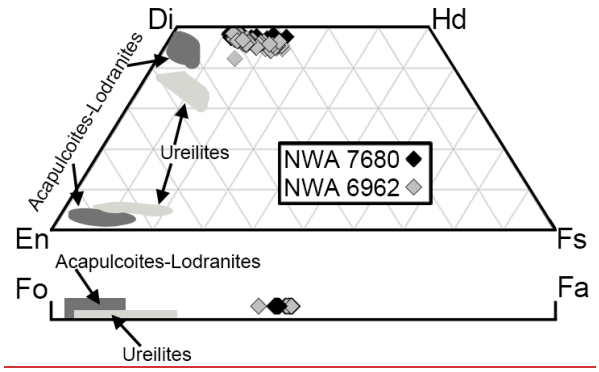

Figure 5. Clinopyroxene (top) and olivine (bottom) major element compositions for NWA 7680 and NWA 6962. Mineral short forms are as follows: diopside (Di), hedenbergite (Hd), enstatite (En), ferrosilite (Fs), forsterite (Fo), fayalite (Fa). Ranges of compositions for ureilites, acapulcoites and lodranites are also shown from Goodrich et al. (2011) and references therein.

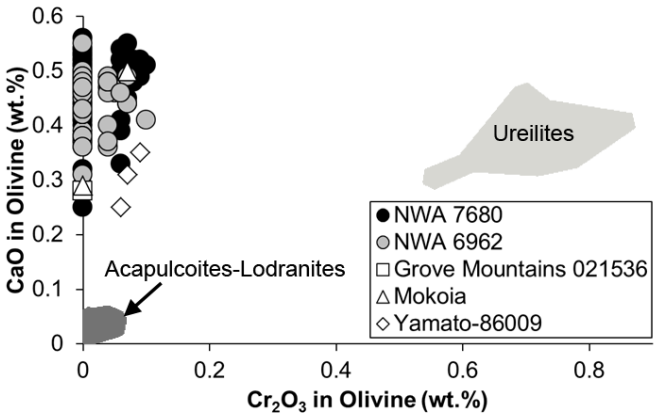

Figure 6. CaO and Cr_2O_3 content of olivine in NWA 7680 and NWA 6962 for comparison with acapulcoites-lodranites and ureilites (Goodrich and Righter 2000 and references therein), a Grove Mountains 021536 clast (Zhang et al. 2010) and clasts in Mokoia and Yamato-86009 (Jogo et al. 2013).

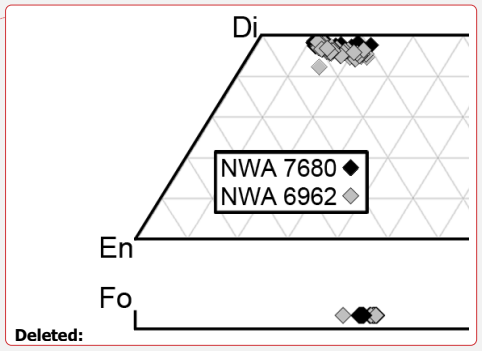

Deleted: Figure 5. Clinopyroxene (top) and olivine (bottom) major element compositions for NWA 7680 and NWA 6962. Mineral short forms are as follows: diopside (Di), hedenbergite (Hd), enstatite (En), ferrosilite (Fs), forsterite (Fo), fayalite (Fa).¶

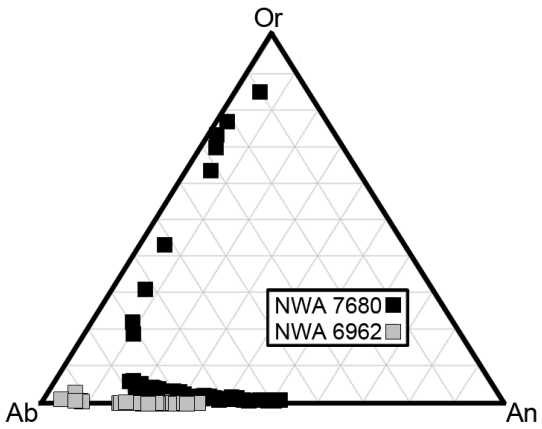

Figure 7. Feldspar major element compositions for NWA 7680 and NWA 6962.

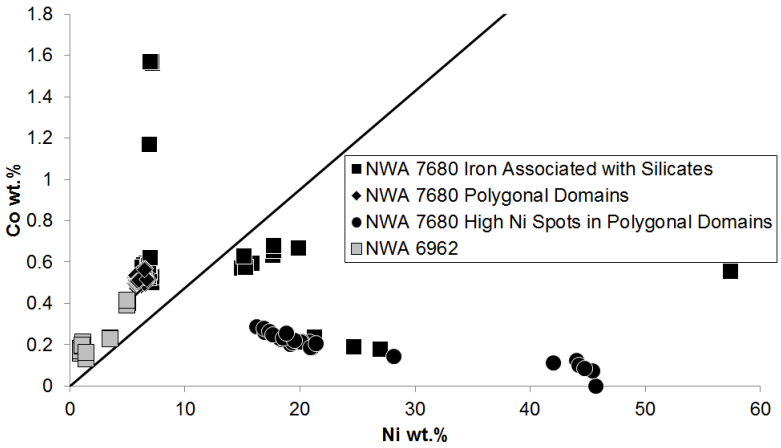

Figure 8. Co and Ni concentrations for metal components in NWA 7680 and NWA 6962. The solid line represents the primitive solar ratio (e.g., Davidson et al., 2014).

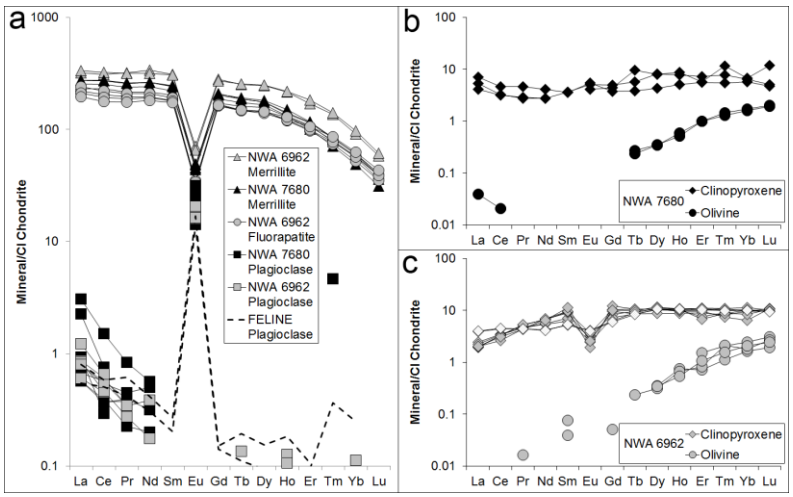

Figure 9. Rare earth element compositions for a) Phosphates and plagioclase, b) NWA 7680 pyroxene and olivine, and c) NWA 6962 pyroxene and olivine. Note in a) compositions from the feldspar-nepheline (FELINE) clast found in the Parnallee LL 3.6 chondrite are also shown (Bridges et al., 1995). In c) data that are not uniform grey are pyroxene grains formed as replacement of olivine (See Figure 2d). CI chondrite normalization values from McDonough and Sun (1995).

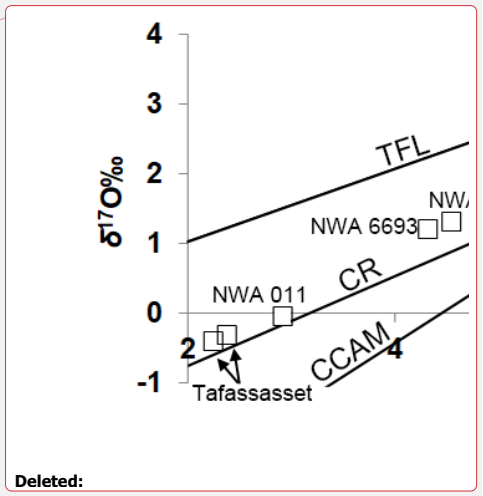

Deleted:

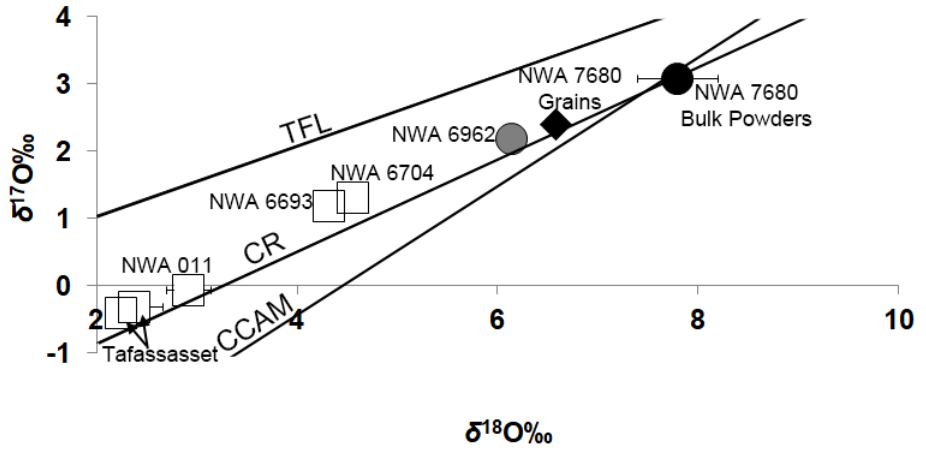

Figure 10. Oxygen isotope values for NWA 7680 bulk powders and grains compared to other carbonaceous achondrites and relevant carbonaceous chondrite trends. Compositions are shown from NWA 6962, NWA 6704, NWA 6693, NWA 011 and Tafassasset (Floss et al. 2005; Gardner-Vandy et al. 2012; Irving et al. 2013; Warren et al. 2013; Hibiya et al. 2019). The carbonaceous chondrite anhydrous mineral (CCAM) line is drawn from data in Clayton and Mayeda (1999) and the CR chondrite trend is a best fit line from the data of Schrader et al. (2014) and references therein. Unless indicated, the 2 SE values are within the areas of the symbols.

Deleted: **Figure 10.** Oxygen isotope values for NWA 7680 bulk powders and grains compared to other carbonaceous achondrites and relevant carbonaceous chondrite trends. Compositions are shown from NWA 6962, NWA 6704, NWA 6693, NWA 011 and Tafassasset (Floss et al. 2005; Gardner-Vandy et al. 2012; Irving et al. 2013; Warren et al. 2013; Hibiya et al. 2019). The carbonaceous chondrite anhydrous mineral (CCAM) line and CR chondrite trend are drawn from data in Clayton and Mayeda (1999).¶

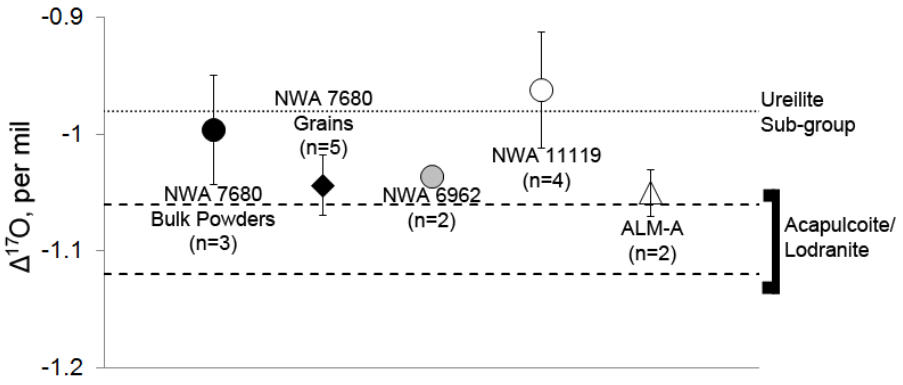

Figure 11. Average oxygen isotope values for NWA 7680 bulk powders and grains. Compositions for the achondrites NWA 6962 (Irving et al., 2013), NWA 11119 (Srinivasan et al., 2018), ALMA-A (Bischoff et al., 2014), ureilites (Rumble et al., 2010) and acapulcoites/lodranites (Greenwood et al., 2012) are shown for comparison. Error bars represent 2 SE and *n* denotes the number of analyses.

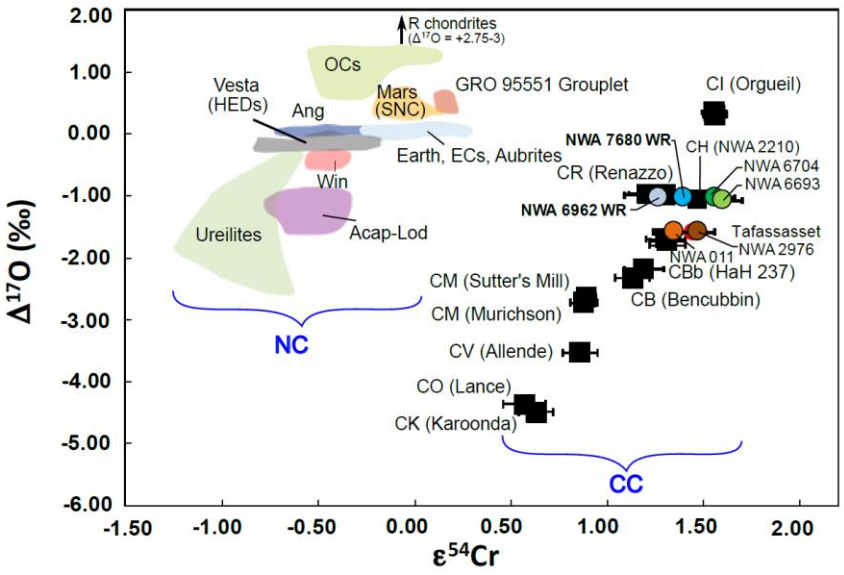

Figure 12. $\varepsilon^{54}Cr$ vs. $\Delta^{17}O$ diagram showing whole rock NWA 7680 and NWA 6962 compositions in comparison to other achondrite and chondrite meteorites. Literature data are from Sanborn et al. (2019) and references therein. $\Delta^{17}O$ data for NWA 6962 from Irving et al. (2013). The plot shows two distinct groupings: the carbonaceous chondrite-like materials (CC) and the non-carbonaceous materials (NC).

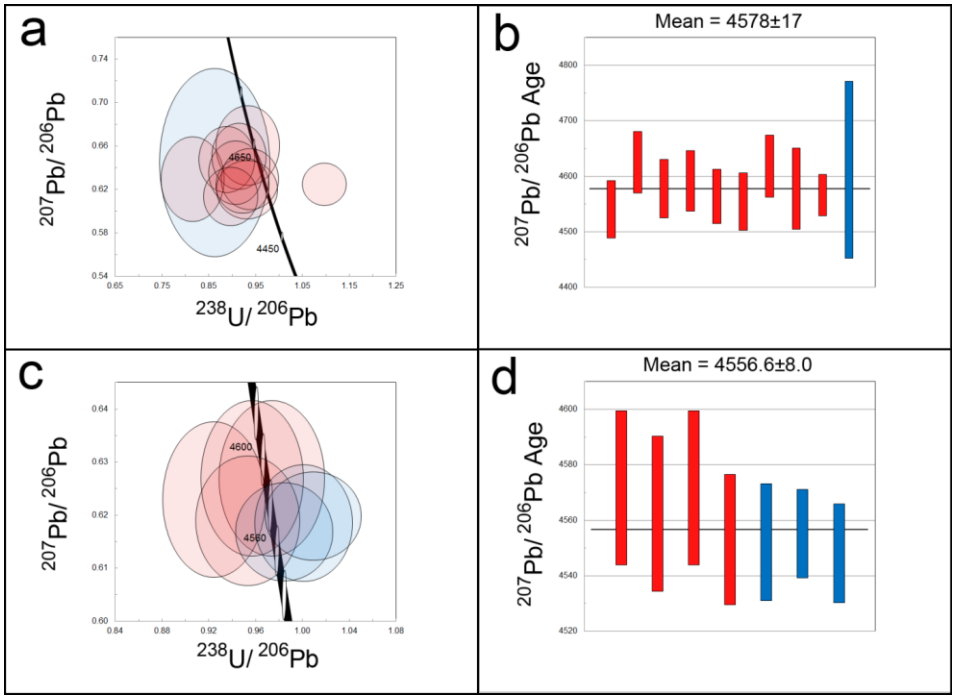

Figure 13. Tera-Wasserburg plots of phosphate data from a) NWA 7680 and c) NWA 6962. Corresponding data used for weighted mean ^{207}Pb-^{206}Pb age shown in b) NWA 7680 and d) NWA 6962. Red data is from merrillite and blue data is from fluorapatite. All uncertainties are 2σ.

Deleted: 12

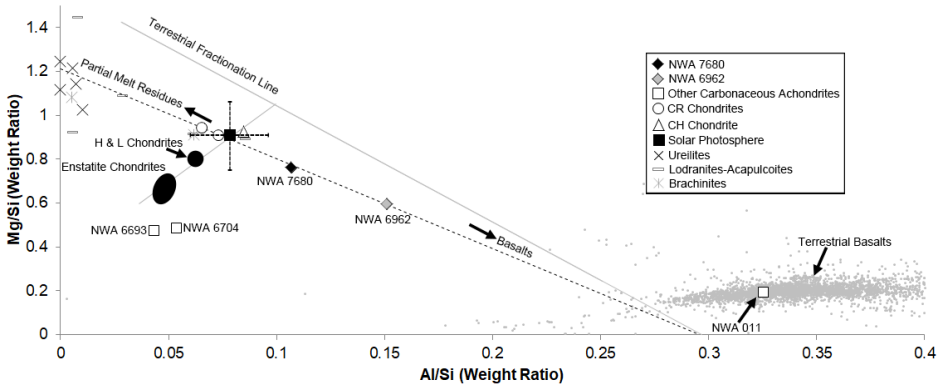

Figure 14. Plot of modal recombination compositions for NWA 7680 and NWA 6962. A dotted trend line is drawn through CR chondrite data, NWA 7680 and NWA 6962. An arrow indicates the direction where fractionation would lead to a roughly basaltic melt composition. CH chondrite and CR chondrite data taken from Ivanova and Petaev (2015) and Weisberg et al. (1993) and references therein. Compositions from the carbonaceous achondrites NWA 6704, NWA 6693 and NWA 011 are taken from Hibiya et al. (2019), Warren et al. (2013) and Yamaguchi et al. (2002) respectively. Ureilite, lodranite-acapulcoite and brachinite compositions are given for comparison (Jarosewich, 1990 and references therein; Mittlefehldt et al., 1998 and references therein). The cosmochemical trend line (through chondritic compositions) and the terrestrial fractionation line are modified from Jagoutz et al. (1979) and Righter et al. (2006) and references therein. Terrestrial basalt compositions were downloaded from PetDB (www.earthchem.org/petdb) on 7, July 2019. The parameters used to acquire the data are found in the Supporting Information online.

Deleted: 13

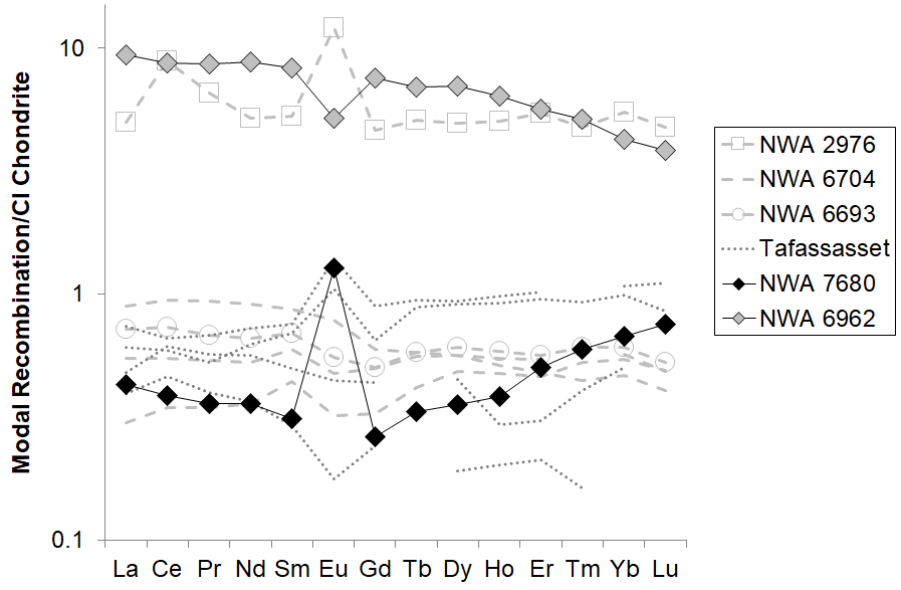

Figure 15. Rare earth element patterns calculated from modal recombinations of constituent minerals (whole rock equivalent) in NWA 7680 and NWA 6962. These compositions are compared with NWA 2976 (Bouvier et al. 2011), NWA 6704 and NWA 6963 (Hibiya et al. 2019) and Tafassasset (Gardner-Vandy et al. 2012; Göpel et al. 2015). CI chondrite normalization values are taken from McDonough and Sun (1995).

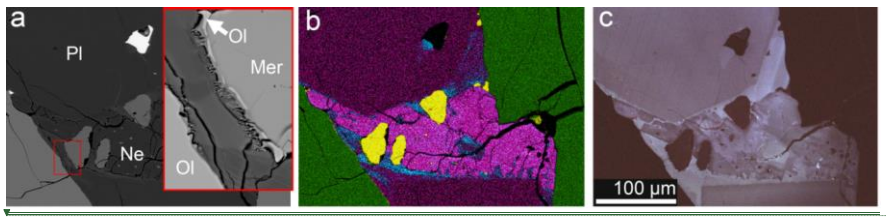

Figure 16. a) BSE image of NWA 7680 showing late-stage melt intrusion between two large plagioclase crystals and two large olivine crystals. Inset image shows close-up of merrillite grain that has been broken off of surrounding olivine during the melt intrusion. b) Chemical map of the same region highlighting Mg (green), Na (purple), P (yellow) and K (blue). c) RGB-UV CL

Moved down [1]:

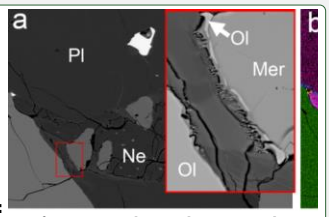

Figure 14. a) BSE image of NWA 7680 showing late-stage melt intrusion between two large plagioclase crystals and two large olivine crystals. Inset image shows close-up of merrillite grain that has been broken off of surrounding olivine during the melt intrusion. b) Chemical map of the same region highlighting Mg (green), Na (purple), P (yellow) and K (blue). c) RGB-UV CL image showing primary structure in the large plagioclase grains, new growth along edges and mottled melt intrusion.¶

Deleted: ¶

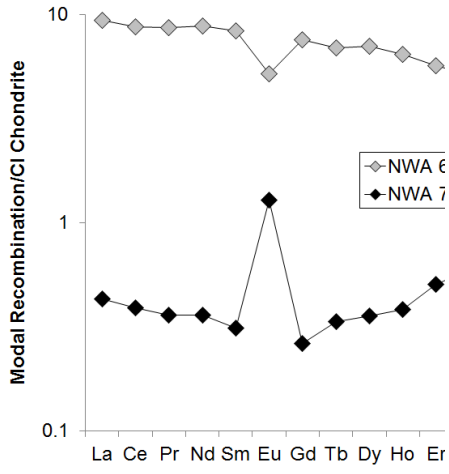

Deleted: **Figure 15**. Rare earth element patterns calculated from modal recombinations of constituent minerals (whole rock equivalent). CI chondrite normalization values are taken from McDonough and Sun (1995).¶

Moved (insertion) [1]

Deleted: 4

image showing primary structure in the large plagioclase grains, new growth along edges and mottled melt intrusion.